Weather and Climate Extremes 45 (2024) 100716

Contents lists available at ScienceDirect

Weather and Climate Extremes

journal homepage: www.elsevier.com/locate/wace

The key role of extreme weather and climate change in the occurrence of exceptional fire seasons in south-central Chile

Tomás Carrasco-Escaff[a,*], René Garreaud[a,b], Deniz Bozkurt[a,c,g], Martín Jacques-Coper[a,d,g], Aníbal Pauchard[e,f]

[a] Center for Climate and Resilience Research (CR)[2], Santiago, Chile
[b] Departamento de Geofísica, Universidad de Chile, Santiago, Chile
[c] Departamento de Meteorología, Universidad de Valparaíso, Valparaíso, Chile
[d] Departamento de Geofísica, Universidad de Concepción, Concepción, Chile
[e] Laboratorio de Invasiones Biológicas (LIB). Facultad de Ciencias Forestales, Universidad de Concepción, Concepción, Chile
[f] Institute of Ecology and Biodiversity (IEB), Concepción, Chile
[g] Center for Oceanographic Research COPAS Coastal, Universidad de Concepción, Chile

ARTICLE INFO

Keywords:
Wildfire
Extreme weather
Climate change
Attribution
Chile

ABSTRACT

Unprecedentedly large areas were burned during the 2016/17 and 2022/23 fire seasons in south-central Chile (34-39°S). These seasonal-aggregated values were mostly accounted for human-caused wildfires within a limited period in late January 2017 and early February 2023. In this paper, we provide a comprehensive analysis of the meteorological conditions during these events, from local to hemispheric scales, and formally assess the contribution of climate change to their occurrence. To achieve this, we gathered monthly fire data from the Chilean Forestry Corporation and daily burned area estimates from satellite sources. In-situ and gridded data provided near-surface atmospheric insights, ERA5 reanalysis helped analyze broader wildfire features, high-resolution simulations were used to obtain details of the wind field, and large-ensemble simulations allowed the assessment of climate change's impact on extreme temperatures during the fires. This study found extraordinary daily burned area values (>65,000 ha) occurring under extreme surface weather conditions (temperature, humidity, and winds), fostered by strong mid-level subsidence ahead of a ridge and downslope winds converging towards a coastal low. Daytime temperatures and the water vapor deficit reached the maximum values observed across the region, well above the previous historical records. We hypothesize that these conditions were crucial in exacerbating the spread of fire, along with longer-term atmospheric processes and other non-climatic factors such as fuel availability and increasing human-driven ignitions. Our findings further reveal that climate change has increased the probability and intensity of extremely warm temperatures in south-central Chile, underscoring anthropogenic forcing as a significant driver of the extreme fire activity in the region.

1. Introduction

Wildfires pose severe threats to human society and terrestrial ecosystems (Paveglio et al., 2015; Bowman et al., 2020; Grillakis et al., 2022), with direct impacts in terms of health effects, environmental degradation, loss of biodiversity and detrimental economic implications, among others (Kochi et al., 2010; Youssouf et al., 2014; Liu et al., 2015; Kelly et al., 2020; Xu et al., 2020). In the last decades, fire activity has increased within ecoregions most vulnerable to wildfire disasters, regardless of fire-fighting capacity or management tactics (Bowman et al., 2009; Abatzoglou and Williams, 2016; Williams et al., 2019; Weber and Yadav, 2020; Duane et al., 2021; Ellis et al., 2022). Moreover, wildfires of unprecedented size, intensity, and duration have devastated several territories worldwide in recent years (Turco et al., 2019; Richardson et al., 2021; Giannaros et al., 2022; Ramos et al., 2023; Rodrigues et al., 2023), underscoring the urgent need to improve understanding of this phenomenon at global and regional scales, including their climate drivers.

Along the subtropical west coast of South America, south-central Chile (34-39°S; see Fig. 1) is recognized as a fire-prone region due to a

* Corresponding author.
E-mail address: tcarrasco@dgf.uchile.cl (T. Carrasco-Escaff).

https://doi.org/10.1016/j.wace.2024.100716
Received 12 April 2024; Received in revised form 8 July 2024; Accepted 15 August 2024
Available online 16 August 2024

complex interplay of climatic, human, and biological factors. Characterized by a north-south transition from a Mediterranean to a temperate climate, the region receives more than 70% of the precipitation during winter (Boisier et al., 2018) and exhibits dry and warm summers, which fosters favorable climate conditions for wildfires. Its vegetation encompasses a mix of native plant communities (i.e., matorral shrublands, deciduous and evergreen forests), non-native tree plantations (especially *Pinus radiata* and *Eucalyptus globulus*), and other mixed vegetation types dominated by non-native grasses, shrubs, and trees (Schulz et al., 2010; Miranda et al., 2017). Between 1985 and 2016, the fire regime in this region was characterized by burned area values per fire season (from July to June, peaking between December and February) in the range of 10,000–100,000 ha, with an average of ~36,000 ha, and fire number per season in the range 2300–6000 (CONAF, 2023). Year-to-year variations in the seasonal burned area across this region are partly modulated by climate variability, especially by the concurrent spring/summer air temperature and the preceding winter/spring precipitation (González and Veblen, 2006; González et al., 2011; Holz et al., 2012, 2017; Urrutia-Jalabert et al., 2018). Consistently, studies have shown that El Niño-Southern Oscillation (ENSO) and the Antarctic Oscillation (AAO) influence seasonal fire activity in the region (Holz et al., 2012; Urrutia-Jalabert et al., 2018; Cordero et al., 2024). Furthermore, south-central Chile has experienced a long-term drying trend in the last decades along with an increase in the frequency of heatwaves (Boisier et al., 2018; González-Reyes et al., 2023), fostering conditions that promote large fires in the region (McWethy et al., 2021). Since 2010, south-central Chile has undergone an extended period of drought (Garreaud et al., 2017, 2020), increasing fire activity (González et al., 2018).

The fire regime described before was exceeded during the 2016/2017 fire season, with more than 500,000 ha consumed by fires, marking the most extensive fire season on record (CONAF, 2023). The abnormal seasonal fire activity was primarily concentrated in late January 2017, when a megafire (>10,000 ha; see Linley et al. (2022) for a discussion on fire nomenclature) was active in the region. On January 20th, the Las Máquinas fire complex started in the administrative region of Maule (Fig. 1a), consuming nearly 160,000 ha in the following days and resulting in the largest wildfire ever recorded in Chile (CONAF, 2023). During the following years, the fire activity remained within the historical range until the 2022/23 season, when the burned area saw a new dramatic rise, exceeding 400,000 ha, mainly during the first week of February 2023. During that period, the Santa Ana fire complex ignited in the administrative region of Biobio (Fig. 1b) and consumed nearly 69,000 ha in the following days (CONAF, 2023), becoming one of the largest wildfires in south-central Chile. In both events, large areas of forestry plantations of non-native *Eucalyptus* spp. and *Pinus radiata*, along with native vegetation and other mixed agriculture and abandoned fields were burnt (McWethy et al., 2018; Bowman et al., 2019). The damage to local ecosystems included the loss of endemic flora and fauna and the reduction of the already threatened native ecosystems (McWethy et al., 2018). There were also significant economic costs for small farmers, big forestry companies, and urban and periurban areas.

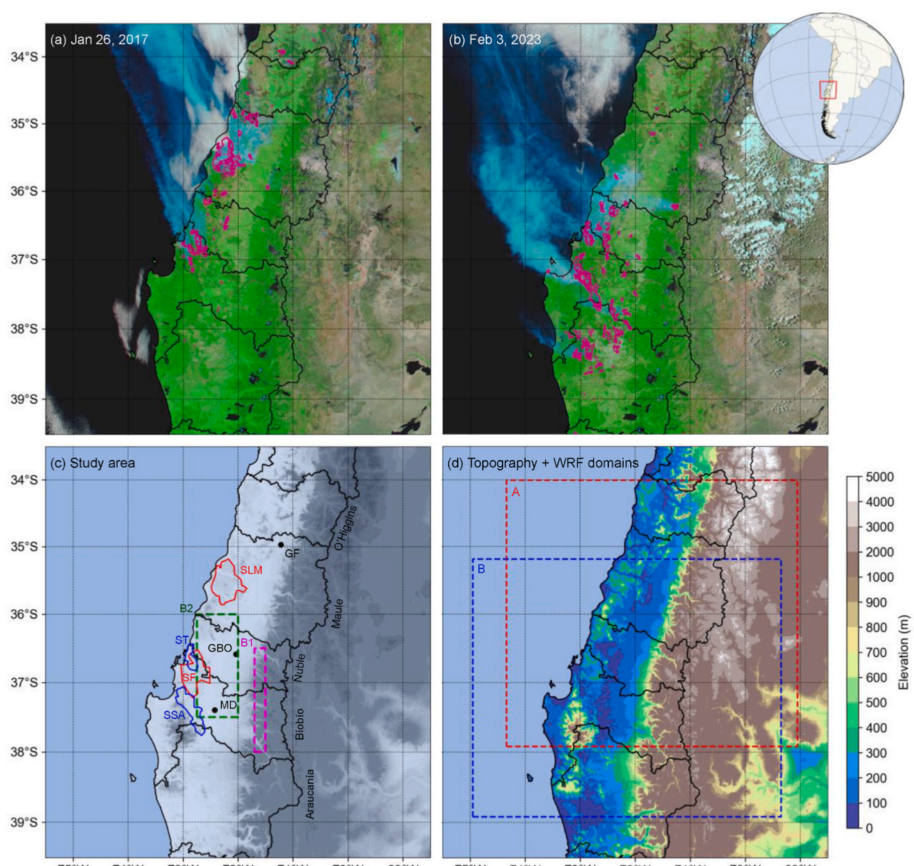

Fig. 1. (a) MODIS Aqua satellite image (corrected reflectance, bands 7-2-1) of south-central Chile on Jan 26, 2017. The polygons in violet show the area burned for three days around Jan 26, 2017. (b) The same as (a) but for Feb 03, 2023. (c) Location of the main sectors, boxes, administrative regions, and weather stations referenced in this work, including Sector Las Máquinas (SLM, upper red polygon), Sector Florida (SF, lower red polygon), Sector Tomé (ST, upper blue polygon), Sector Santa Ana (SSA, lower blue polygon), Box 1 (B1, box in fuchsia), Box 2 (B2, box in green), weather station General Freire (GF, upper black dot), General Bernardo O'Higgins (GBO, middle black dot), and María Dolores (MD, lower black dot). (d) Topography from the GTOPO30 Digital Elevation Model (~1 km spatial resolution) along with WRF inner domains defined for studying the atmospheric conditions during a week around Jan 26, 2017 (domain A), and Feb 03, 2023 (domain B). (For interpretation of the references to color in this figure legend, the reader is referred to the Web version of this article.)

More tragically, more than thirty fatalities were reported as a result of these events (SENAPRED 2024a, 2024b). Post-fire investigations point to human-induced ignitions, although it has not been established if they were accidently or intentionally (arson).

These seasons concentrated their anomalous fire activity within a limited time frame, suggesting a key role of short-term atmospheric processes in the intensity and spread rate of the fire. A few previous studies have explored the role of meteorological conditions in the extreme fire events in south-central Chile during late January 2017 and early February 2023. Bowman et al. (2019) reported extreme fire weather during the second half of January 2017, with regional-wide daily values of maximum temperature and wind speed above the 95th percentile, including the highest temperature on their dataset. Cordero et al. (2024) showed that exceptionally fire weather conditions were experienced in the region during February 2023, highlighting the role of dry downslope winds (locally known as *Puelche*).

Despite these efforts, the meteorological mechanisms -from local to hemispheric scales-underpinning the extreme fire events in south-central Chile during late January 2017 and early February 2023 remain unclear. Moreover, a formal quantification of the impact of climate change on such weather conditions is still lacking in the scientific literature, as well as a robust assessment of their potential predictability. The purpose of this investigation is to fill these gaps. To achieve its goal, this study analyzes daily estimates of regional-wide burned area and concurrent surface weather conditions, explores the main meteorological mechanisms involved from local to hemispheric scales, and assesses the potential impact of climate change in the extreme weather observed during the mentioned periods. This paper is organized as follows: Sect. 2 presents the study area, Sect. 3 describes the data and methods, Sect. 4 presents the results of this study, and Sect 5 and 6 discusses and summarizes the results, respectively.

2. Study area

2.1. Bio-geographic context

The study area encompasses the Chilean continental territory between 34 and 39°S (hereafter south-central Chile; see Fig. 1c), a strip of land less than 200 km wide between the Pacific coast and the Andes Cordillera. A coastal range runs almost continuously, separating the inland central valley from the sea border. South-central Chile includes five administrative regions (from O'Higgins to La Araucanía) and concentrates ~25% of the country's population (>5 million inhabitants according to Instituto Nacional de Estadísticas (2023)). It hosts native ecosystems with high species diversity and endemism (Myers et al., 2000; Echeverría et al., 2006). Natural vegetation ranges from matorral shrublands and woodlands of sclerophyllous species to the north to evergreen species to the south, with deciduous *Nothofagus* species dominating higher elevations in the coastal range and Andes Cordillera (Luebert and Pliscoff, 2006). Since the 1970s, the study area has undergone a rapid land use and cover change (LUCC; Schulz et al., 2010; Miranda et al., 2017), with most of the native forest replaced with industrial forestry plantations of non-native species such as *Pinus radiata* and *Eucalyptus* spp. These plantations cover up to 90% of some landscapes, especially in the Coastal Range (Echeverría et al., 2006; Nahuelhual et al., 2012; McWethy et al., 2018). Along with agricultural abandonment and the expansion of human activity near cities and on the urban-rural interface, the plantation expansion has increased the fire risk (fuel loads, ignition, and flammability) in the study area (Carmona et al., 2012; Díaz-Hormazábal and González, 2016; Taylor et al., 2017). Moreover, the massive conversion of native vegetation to forestry plantations and the spread of other invasive trees (e.g. Acacia dealbata, Acacia melanoxylon) and shrubs species (e.g. *Genista monspessulana*, Ulex europaeus) have altered the fuel structure (amount and connectivity of biomass) by creating large homogeneous patches of the same single species, increasing the risk of catastrophic fires (Pauchard et al., 2008; González et al., 2011; Cóbar-Carranza et al., 2015).

2.2. Fire-climate background

South-central Chile features a climate transition from semiarid, Mediterranean conditions northward to more humid and temperate conditions southward, with winter-to-annual precipitation ratios ranging from 90% to 70% in the north-south direction (Boisier et al., 2018). This marked rainfall seasonality increases the amount of burnable biomass during winter/spring and turns vegetation flammable during the subsequent warm and dry summer (December, January, and February), fostering a fire-prone environment. Most fire activity throughout Chilean territory occurs in south-central Chile, with a significant increase in intensity during the austral summer (González et al., 2018).

The fire regime in this area is characterized by a burned area of ~36,000 ± 26,000 ha (mean ± std. dev.) per fire season (July to June) and an occurrence of ~3 900 ± 900 fires on average per fire season (period 1985–2016; CONAF, 2023). Most of the burned area is accounted for by a few large fires (>200 ha), while the total number of fires is primarily explained by small fires (<5 ha) (González et al., 2020). Likewise, it is estimated that over 98.5% of the fires in south-central Chile are caused by humans, either intentionally (36.6%) or accidently (58.2%) (Pozo et al., 2022). While lightning is a natural ignition source for many wildfires worldwide (e.g., Wierzchowski et al., 2002; Larjavaara et al., 2005; Campos et al., 2024), and this threat is expected to increase in the future (e.g., Pérez-Invernón et al., 2023), this factor is quite infrequent in Chile as the Andes cordillera inhibits the development of convective storms in the central valley (Viale and Garreaud, 2014).

Except for the coastal strip, south-central Chile has been warming during the last four decades at approximately 0.2°/decade (e.g., Falvey and Garreaud, 2009), most notably in maximum temperatures during summer. Consistently, the study area is characterized by the increasing occurrence of warm events, including heatwaves (>0.75 events per decade) (Piticar, 2018; González-Reyes et al., 2023), a trend that is expected to continue in the future (Feron et al., 2019). Warm events in the study area typically occur when an upper-level ridge and surface anticyclone approach southern Chile, thus extending the semi-permanent high-pressure cell over the subtropical Southeast Pacific to about 40°S. Under these conditions, the sea level pressure (SLP) along the coast increases poleward (reversing the climatological gradient), driving low-level offshore flow in central Chile, which in turn forces subsidence over the western slope of the Andes. The easterly, downslope wind is locally known as *Puelche* (Montecinos et al., 2017) and, together with the large-scale subsidence, results in low-level warming over the central valley and coastal zone. The offshore displacement of the cool marine boundary layer produces a coastal low off central Chile that further reinforces the reversal of the SLP gradient and easterly winds (Garreaud et al., 2002). Such a synoptic pattern resulting in heatwaves in south-central Chile is favored by hemispheric-scale Rossby wave trains emanating from the tropical western Pacific and Indian Ocean, as documented by Demortier et al. (2021) and Jacques-Coper et al. (2021).

3. Data and methods

3.1. Observational data

Monthly statistics of burned area and fire occurrence for administrative regions from O'Higgins to La Araucanía were obtained from the Chilean Forestry Corporation (Corporación Nacional Forestal (CONAF); CONAF, 2023). Additionally, we estimated daily values of burned area for south-central Chile from the Terra and Aqua combined MCD64A1 Version 6.1 Burned Area product (Giglio et al., 2021). The MCD64A1 employs 500-m Moderate Resolution Imaging Spectroradiometer (MODIS) imagery coupled with 1-km MODIS active fire observations to identify the burn date for 500-m grid cells by locating the occurrence of rapid changes in daily surface reflectance time series data. The algorithm maps the spatial extent of recent fires to derive burned area estimates.

Daily maximum temperature (Tx) time series from three weather stations with five-decades long, quality-controlled records in south-central Chile were acquired from the Chilean weather service (Dirección Meteorológica de Chile, DMC; see Fig. 1c). Of these stations, General Bernardo O'Higgins (GBO), situated at 36.59°S, 72.04°W, is the closest to the locations of the extreme fire outbreaks and is primarily utilized in our analysis. In addition, Tx observations from more than 150 stations during the two weeks around the outbreaks were obtained from the Center for Climate and Resilience Research (CR2) meteorological viewer (VisMet; https://vismet.cr2.cl/). Of these stations, Cauquenes (35.96°S, 72.29°W) and Los Angeles (37.44°S, 72.52°W) were used along with GBO to validate WRF simulations. Furthermore, Tx gridded data were obtained from the observational-based dataset CR2Met version 2.5 (Alvarez-Garreton et al., 2018) and the fifth-generation ECMWF reanalysis (ERA5; Hersbach et al., 2020). CR2Met has a spatial resolution of 0.05° and is based on *in-situ* observations for the Chilean continental territory, the near-surface temperature provided by the ERA5, and land surface temperature estimates from MODIS satellite retrievals.

To characterize the synoptic conditions associated with the extreme fire outbreaks and their severity, we utilized sea level pressure (SLP), 10-m wind speed, and geopotential height and vertical velocity at 500 hPa (Z500 and ω_{500}, respectively) from the ERA5 dataset. These data, spanning from 1979 to 2023, were analyzed at a 6-h temporal resolution on a 0.25° × 0.25° latitude-longitude grid. Vapor-pressure deficit (VPD) was derived from hourly values of dew point temperature and air temperature from the ERA5 from 1979 to 2023 by computing the saturated and actual water vapor pressure and then taking their difference. Additionally, Z500 and 0.2101 sigma streamfunction anomalies (with respect to 1991–2020 climatology) computed from the NCEP-NCAR Reanalysis 1 (Kalnay et al., 1996) were provided by the NOAA PSL, Boulder, Colorado, USA, from their website at https://psl.noaa.gov, to assess mid and upper-troposphere features at hemispheric scale.

We used the 2-m air temperature and 10-m wind speed forecast at 0.25° × 0.25° lat-lon resolution produced by the Global Forecast System (GFS; National Centers for Environmental PredictionNational Weather ServiceNOAA & U.S. Department of Commerce, 2015) to assess forecasts of extreme surface conditions. GFS currently has four initializations per day (00, 06, 12, and 18 UTC) and is integrated for two weeks. The data was obtained from NCAR's Research Data Archive (RDA) using the THREDDS data server and Python's Siphon library. We used grid cell values at 36.5°S-72°W (central valley) because of its proximity to the largest fires and the availability of measurements at GBO.

3.2. Regional model simulations

To conduct our atmospheric simulations, the Weather Research and Forecasting (WRF) Advanced Research WRF (ARW) version 4.3.2 Model (Skamarock and Klemp, 2008; Skamarock et al., 2019) was utilized. The model was configured with a nested domain approach, comprising three domains with grid spacing of 18 km, 9 km, and 2 km, and 60 vertical levels. For the 2023 case, the simulation spanned from February 1, 2023, at 00:00 UTC to February 7, 2023, at 00:00 UTC. The 2017 case was simulated from January 23, 2017, at 00:00 UTC to January 29, 2017, at 00:00 UTC. The initial and lateral boundary conditions were obtained from the ERA5 reanalysis data at 6-h intervals with a grid spacing of 0.25°. ERA5 sea surface temperature fields, initial soil parameters (soil water, moisture, and temperature), and surface pressure and skin temperatures were used as surface boundary conditions for the mother domain.

Both the 2023 and 2017 simulations employed the same set of parameterization schemes. Microphysical processes were represented using the Thompson Scheme (Thompson et al., 2008). The Dudhia Shortwave Scheme (Dudhia, 1989) was adopted for shortwave radiation, and the Rapid Radiative Transfer Model (RRTM) Longwave Scheme (Mlawer et al., 1997) was used for longwave radiation. The Noah–MP Land Surface Model (Niu et al., 2011) was implemented to simulate land surface processes. The planetary boundary layer was represented by the Mellor–Yamada Nakanishi Niino (MYNN) scheme (Nakanishi and Niino, 2009). For cumulus physics in the first two domains, the Grell 3D Ensemble Scheme (Grell and Dévényi, 2002) was used, while in the third domain, cumulus processes were explicitly resolved. The selection of specific schemes is based on their demonstrated effectiveness in numerical modeling studies specific to this region, underscoring their applicability despite the scarcity of such applications in the area (Yáñez-Morroni et al., 2018; Schumacher et al., 2020; Arévalo et al., 2023).

3.3. Global model outputs and global climate indices

To quantify the influence of climate change on extreme temperatures in south-central Chile, daily maximum and monthly mean near-surface temperature data were obtained from the NCAR's CESM Large Ensemble (CESM-LE) Project (Kay et al., 2015) which consists of a 40-member single model initial-condition ensemble of fully coupled simulations for the period 1920–2 100 performed with the Community Earth System Model (CESM) version 1 with CAM5.2 as its atmospheric component. Historical radiative forcing is used until 2005, and then the simulations are forced with the RCP8.5 scenario. The project also includes an 1800-year fully coupled control run simulation forced with pre-industrial (1850) radiative conditions (CESM-PI). The simulations have a 1° × 1° lat-lon grid spacing.

We used the GISS Surface Temperature Analysis version 4 (GISTEMP v4; Hansen et al., 2010; Lenssen et al., 2019) to characterize the observed Global Mean Surface Temperature (GMST). We smoothed the GISTEMP data using the Locally Weighted Scatterplot Smoothing (LOWESS; Cleveland, 1979) with a 5-year temporal window to remove the fluctuations in the global mean temperature due to ENSO. In the context of CESM-LE simulations, we represented the observed smoothed Global Mean Surface Temperature (GMST) by modeling it using the ensemble-mean Global Surface Air Temperature (GSAT).

3.4. Statistical method for attribution analysis

A probability-based method for extreme event attribution (EEA; Otto, 2017) was applied to investigate the role of climate change in the occurrence of extreme warm events in south-central Chile. The method involves formulating a statistical model that can correlate the probability distribution of a climate variable of interest with the GMST. By evaluating the model with smoothed GMST anomalies of −1.1, 0.0, and 0.9 °C relative to 2011–2020, we derive the probability distributions corresponding to preindustrial, present-day, and 2 °C above preindustrial climates, respectively. This approach is commonly used in EEA studies to assess changes in the behavior of extreme events due to climate change (e.g., Rivera et al., 2023).

The variable of interest was defined as the highest daily near-surface temperature reached during austral summer (December to February) over south-central Chile (hereafter xTx), and it was computed from the observational-based product CR2Met and the CESM-LE and CESM-PI simulations. To do this, the Tx summer maximum was calculated at each grid point for each dataset. Then, the resulting fields from CESM-LE and CESM-PI simulations were remapped onto the CR2Met grid using the nearest neighbor remapping. After that, we took each dataset's spatial maximum for grid points within south-central Chile. In this way, we obtained one time series from the CR2Met product, one time series from each member of the CESM-LE, and one time series from the CESM-PI run. We compared the CESM-LE and the CR2Met xTx and found a good performance in the representation of the variable of interest, with no statistically significant bias for the period 1991–2020 (Fig. S1).

The CESM-PI xTx was used to determine the probability distribution followed by the variable of interest in a stationary climate. We applied different diagnostics checks to the data and found that xTx closely approximates a normal distribution under stationary conditions (see Fig. S2). Furthermore, we performed a Kolmogorov-Smirnov (K-S) test to check whether there is statistical evidence to reject the hypothesis that the standardized data follows a standard Normal distribution. We obtained a p-value of 0.62, which motivates us to use the normal distribution in the following steps.

We represented xTx in a non-stationary climate by a shifting Normal distribution, where the location parameter varies linearly with the smoothed GMST anomaly relative to 2011–2020 (the covariate), and the scale parameter remains constant. Shift fits are a simple yet robust method for effectively representing temperature extremes in attribution studies utilizing transient simulations (Philip et al., 2020). Thus, our statistical model is:

$$xTx \sim \mathcal{N}(\mu, \sigma^2);\ \mu = \mu_0 + \alpha \bullet GMST' \tag{1}$$

where μ and σ are the location and scale parameters, respectively, μ_0 is the present-day location parameter and α is the trend parameter. The fitting parameters are μ_0, σ and α. We used maximum likelihood estimators (MLE) to fit the model and a 1 000-member non-parametric bootstrap procedure to estimate 95% confidence intervals (CI) on the fit.

We fitted the model to the CR2Met xTx time series and obtained estimates for the fitting parameters. Since the observational-based estimates usually exhibit a large sample uncertainty due to the short record (small sample), we avoid extrapolating distributional parameters for past and future climates and drawing conclusions from observational data. Instead, these results were used only to validate the representation of extremes in the CESM-LE. Thus, we fitted the statistical model to the ensemble of the xTx time series obtained from the CESM-LE and compared the resulting estimates of the fitting parameters against the observational-based estimates. An overlap of the 95% confidence intervals between ensemble and observational-based estimates of the same parameter was interpreted as an acceptable heuristic of both estimations being pooled from the same distribution (e.g., Kharin and Zwiers, 2005; Philip et al., 2020). We do not compare estimates of the trend parameter since the observed trend can be strongly influenced by natural variability.

We defined the class of events under study by using a threshold value z and calculated the present-day return period (τ) as the inverse of the exceedance probability of z in the present-day distribution derived from the CESM-LE. Using the CESM-LE estimates of the fitting parameters, we computed the intensity change of the class of events under study as the difference between the τ return levels obtained from two different distributions (e.g., present-day versus preindustrial). Additionally, we calculated the probability ratio of the class of events under study as the ratio between the exceedance probability of z obtained from two different distributions (e.g., present-day versus preindustrial).

4. Results

4.1. Extreme fire outbreaks in south-central Chile

During the 2016/17 and 2022/23 fire seasons, south-central Chile experienced extraordinary amounts of burned area, exceeding 500,000 ha and 400,000 ha consumed by fires, respectively (Fig. 2a). These values were ~10 times larger than the historical (1985–2016) average. During both seasons, biomass burning was concentrated in a month, contributing to more than 80% of the seasonal burned area.

At a daily scale, burned area values exceeded 20,000 ha between January 21 and January 29, 2017, with an unprecedented peak of over 120,000 ha on January 26, 2017 (Fig. 3a). In 2023, the burned area remained low until February 3, when fire activity suddenly increased and burned above 70,000 ha (Fig. 3c). During the next four days, south-central Chile exhibited burned area values above 40,000 ha.

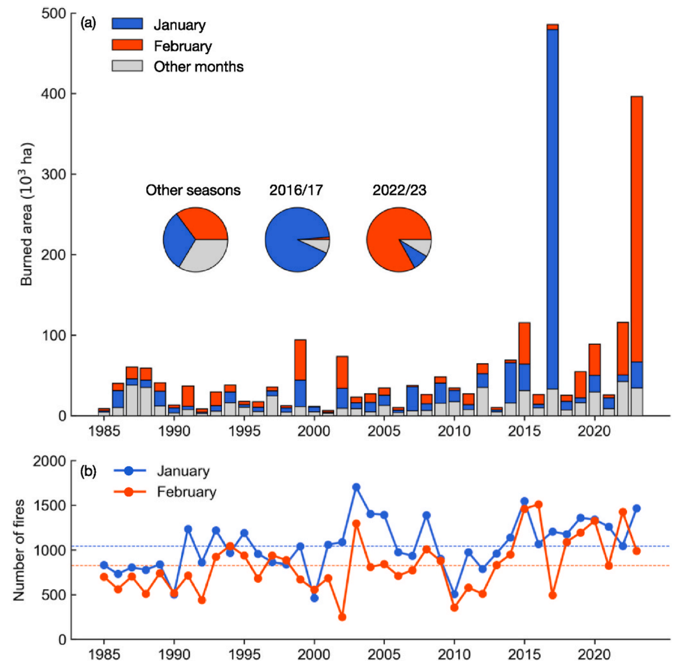

Fig. 2. (a) Time series of burned area per fire season (July–June) in south-central Chile (administrative regions from O'Higgins to La Araucanía) according to CONAF. Colors indicate the burned area in January (blue), February (red), and other months (gray). Insets indicate the percentages of total area burned in January, February, and other months during the 2016/17 and 2022/23 seasons (middle and right chart pies) and other seasons (left chart pie). (b) Time series of number of fires during January (blue) and February (red). Dashed lines indicate mean values. Fire seasons are denoted by their end year. (For interpretation of the references to color in this figure legend, the reader is referred to the Web version of this article.)

In light of the large areas suddenly consumed on January 26, 2017, and February 3, 2023, we focus on the fire outbreaks during those particular days, referred to as FO17 and FO23, respectively. FO17 and FO23 stand out not only for the amounts of the daily burned area but also for the one-day increases in the burned area (~80,000 ha and 65,000 ha, respectively). The spatial extents of the wildfires during three days around FO17 and FO23 are presented in Fig. 1, based on the MODIS burned area product. Both were characterized by a ~300 km band oriented in the north-south direction over the coastal range, with the spatial distribution in 2017 positioned more northerly than that in 2023, possibly since it is unlikely to observe a wildfire where fuels have burned years before.

To quantify the contribution of specific sectors to the burned area statistics, we defined polygons enclosing areas where we observed a rapid increase of burned pixels (Fig. 1), including the locations where the fire complexes of Las Máquinas and Santa Ana occurred. The sectors denoted as Las Máquinas (SLM) and Florida (SF) explained about 65% and 15% of the area consumed during FO17, respectively (Fig. 3a). The sectors denoted as Santa Ana (SSA) and Tomé (ST) contributed to 40% and 15% of the area burned during FO23, respectively (Fig. 3c). Thus, the unprecedented area burnt in the whole 2016/17 and 2022/23 fire seasons was largely accounted for by the wildfires under study that developed in less than ten days -with record expansion on FO17 and FO23- and clustered in specific sectors within south-central Chile. This indicates a highly rapid fire spread under local weather conditions described next.

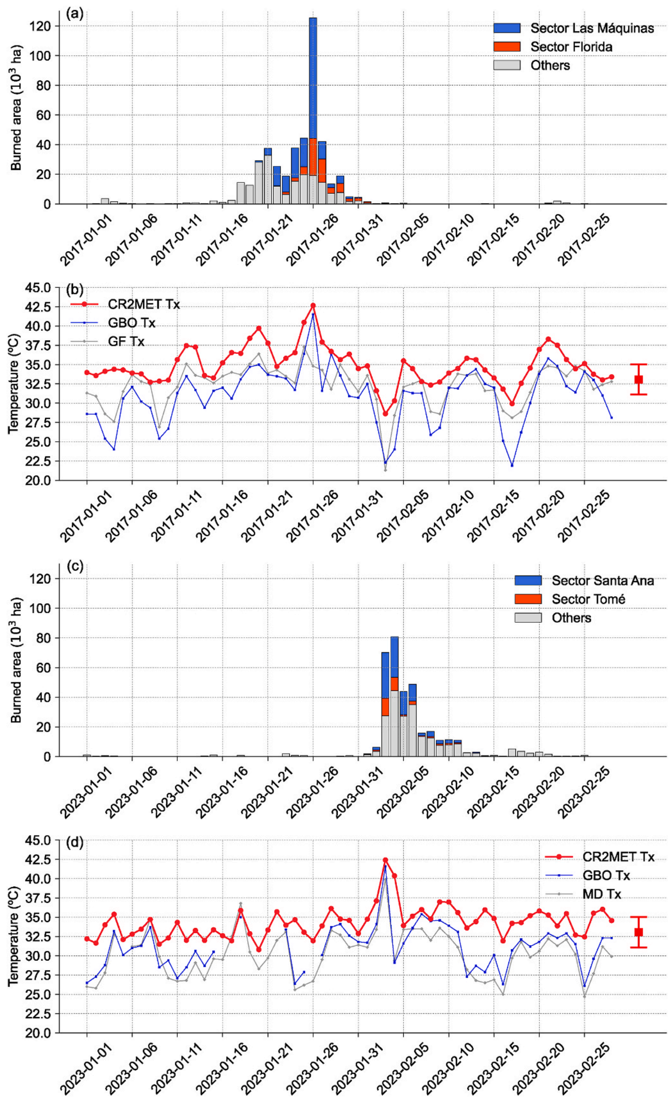

Fig. 3. (a) Daily values of area burned in south-central Chile according to the MODIS MCD64A1 product during January–February 2017. The area burned in sector Las Máquinas, sector Florida, and the rest of the domain are shown in blue, red and gray, respectively. (b) Time series of highest daily maximum temperature in south-central Chile according to CR2Met (CR2Met Tx, red), and daily maximum temperature at weather stations General Bernardo O'Higgins (GBO Tx, blue) and General Freire (GF Tx, gray). The red square with error bars indicates the CR2Met Tx mean for January–February during 1970–2023 plus/minus one standard deviation. (c) The same as (a) but for January–February 2023 and sectors Santa Ana and Tomé. (d) The same as (b) but for January–February 2023 and weather station María Dolores (MD) instead of GF. The locations of weather stations are indicated in Fig. 1. (For interpretation of the references to color in this figure legend, the reader is referred to the Web version of this article.)

4.2. Surface weather conditions

Station records and CR2Met reveal that south-central Chile experienced extremely high temperatures during FO17 and FO23, exceeding 40 °C in several locations (Fig. 3b–d). The spatial patterns of maximum temperatures in three days around FO17 and FO23 show extensive regions of values greater than 40 °C mainly located over the central valley (Fig. 4). The hot core associated with FO17 is positioned more northerly than that associated with FO23, in agreement with the spatial distribution of the wildfires (Fig. 1). The main sectors of fire activity during each event (SLM and SSA) were located on the edge of the zones of highest temperatures.

Using station and gridded data, we quantified the extremity of the temperature values reached during FO17 and FO23. The five-decade measurements of Tx at GBO station show the highest values during FO17 and FO23, with records of 41.5 °C and 41.6 °C, respectively, exceeding the 99th percentile of the empirical distribution by almost 5 °C. At a regional scale, data from the CR2Met show that temperatures during FO17 and FO23 were the highest ever reached in south-central Chile, with values of 42.7 °C and 42.4 °C, respectively (Fig. 5b).

Unlike temperature, there are few weather stations with reliable humidity and wind measurements in the study area. These stations (e.g., GF, GBO, and MD in Fig. 1c) are relatively far from the large fire sectors, so we used the WRF simulations (see Sect. 2.2 for details) to study the evolution of the near-surface variables (note that the WRF runs do not include the possible fire-induced mesoscale patterns). The WRF simulations reasonably reproduce the spatial distribution of the observed temperature field (Fig. 6) and closely follow the air temperature evolution at weather stations near the main regions of fire activity (Fig. 7a and b). Furthermore, the modeled relative humidity, VPD, wind speed, and wind direction at GBO are in agreement with the observations (Fig. S3), supporting the use of the WRF simulations for characterizing the study area.

According to the WRF simulations, low values of relative and specific humidity (below 20% and 6 g/kg, respectively) and high values of VPD (over 60 hPa) were reached near the large fire sectors (SLM and SSA) during FO17 and FO23 (Fig. 7c–f). Similar conditions of relative and specific humidity were observed on other days before and after the fire outbreaks (e.g., January 27, 2017; February 2, 2023). In contrast, VPD reached its maximum value during FO17 and FO23, following closely the evolution of air temperature (Fig. 7e and f). Additionally, based on WRF results, large fire sectors experienced strong *southerly winds* before and during the fire outbreaks, with hourly averages exceeding 25 km/h (Fig. 7g–j). During the afternoon of the outbreaks, a minor zonal component started to develop near the large fire sectors (westerly in the case of FO17 and easterly in the case of FO23), and the following days showed a significant reduction in wind speed. We relate these surface wind conditions in the fire sectors to synoptic scale conditions in the next subsection.

We used ERA5 summer data to compare the extremity of the warm, dry and windy conditions during the fire outbreaks near the main fire sectors (Fig. 8). We computed daily maximum wind speed values from hourly data averaged over an area near the main fire sectors (Box 2 in Fig. 1) and daily maximum VPD from hourly data at the grid point closest to the GBO station. As shown in Fig. 8a, wind speed values surpassed the 95th percentile of the empirical hourly distribution during FO17 and FO23, although they were not unprecedented, as in the case of temperature. On the other hand, our results show that VPD reached its highest and second-highest values during FO17 and FO23, similar to the case of temperature.

The surface weather analysis reveals the occurrence of extreme compound events during FO17 and FO23, including severe warm, dry, and windy conditions near the large fire sectors. As shown by lines of constant water vapor pressure in Fig. 8b, the unprecedented high VPD conditions were primarily driven by the extremely high air temperature, although low moisture content also played a minor role in FO23. In contrast, there is a weak correlation between Tx and daily maximum wind intensities, indicating a degree of independence between temperature and wind speed values near the large fire sectors (Fig. 8a). As a result, Tx values above the 95th percentile tend to occur with moderate to calm winds, implying that the observed combination of warm and windy upper-quantile conditions is relatively infrequently.

Determining whether temperature or wind speed contributed more to the fire spread during FO17 and FO23 would ideally require experiments with fire models, but the present analysis can still provide insights into the relative importance of these meteorological variables. According to Fig. 7, the main fire sectors experienced maximum wind speed

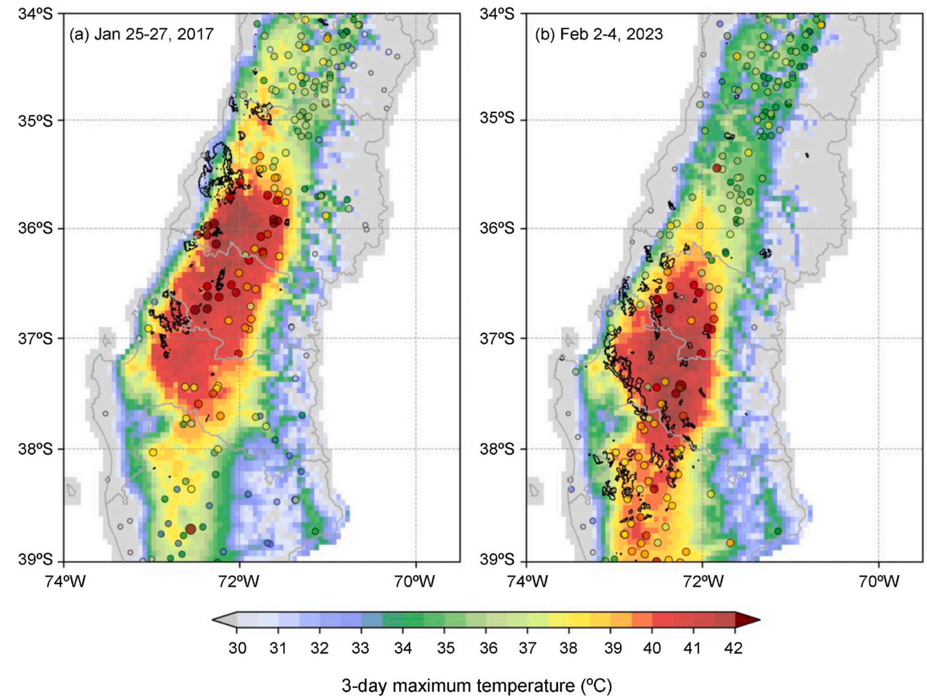

Fig. 4. (a) Spatial distribution of the 3-day maximum temperature around Jan 26, 2017, according to available weather stations (circles) and the CR2Met (gridded data). The polygons in black show the area burned during the three-day period. (b) The same as (a) but for a three-day period around Feb 03, 2023.

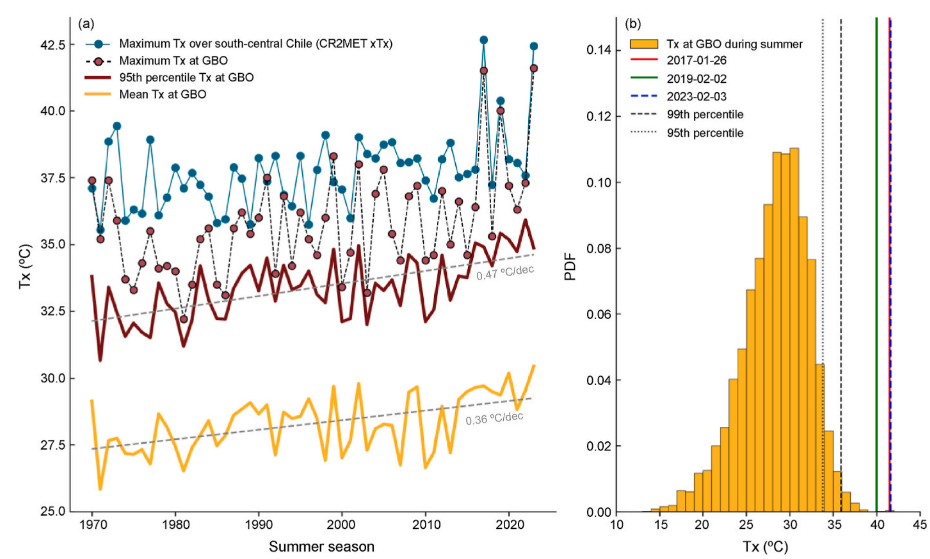

Fig. 5. (a) Mean (yellow line), 95th percentile (dark red line), and maximum (dark red circles) of daily maximum temperature (Tx) during summer (Dec–Feb) at weather station General Bernardo O'Higgins (GBO; see Fig. 1) from 1970 to 2023. Green circles indicate the highest summer temperature in south-central Chile (xTx) according to the CR2Met. (b) Empirical frequency distribution of daily maximum temperature at GBO for summer days from 1970 to 2023. Summer seasons are denoted by their end year. (For interpretation of the references to color in this figure legend, the reader is referred to the Web version of this article.)

values (relative to the 7-day simulation period) during the days before the fire outbreaks. As revealed by Fig. 3a–c, active wildfires were already present in the main fire sectors during these days (Jan 25, 2017, and Feb 2, 2023); nonetheless, the unprecedented values of the burned area did not occur until the next day, during the temperature maxima (Jan 26, 2017, and Feb 3, 2023). Although non-climatic factors could have played a role in the more rapid fire spread during the temperature maxima compared to the wind maxima, the significant differences in the daily burned area between the fire outbreaks and the days before them suggest a more substantial contribution of extremely high temperatures to the fire spread in comparison to wind speed.

Given the prominent role of local meteorological conditions in creating an environment suitable for the extremely large expansion of the wildfires around FO17 and FO23, it is pertinent to determine whether or not the current generation of numerical weather forecasts can anticipate extreme conditions. Given the significant contribution of temperature and wind to the occurrence of the fire outbreaks, we explored the 2-m air temperature and 10-m wind speed forecast produced by the GFS at the grid point closest to GBO station. Fig. 9 shows the 15-day forecast at 18 UTC (close to the time of maximum temperature and wind speed) initialized at 06 and 18 UTC several days before FO17 and FO23. The upper row corresponds to the observations at GBO.

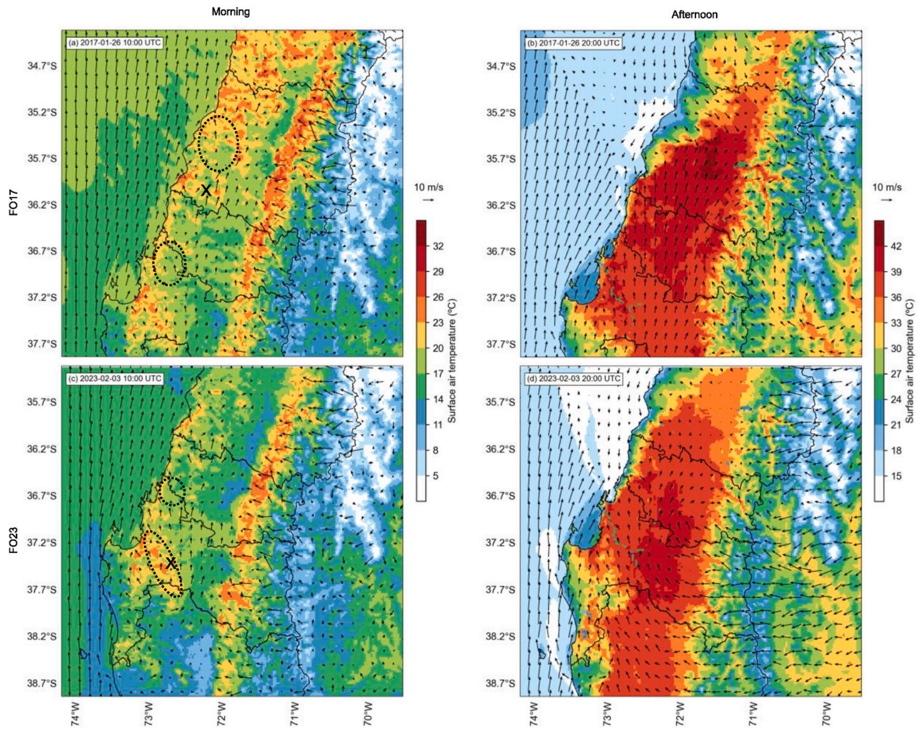

Fig. 6. Near-surface air temperature and horizontal winds from WRF simulations for (a) Jan 26, 2017, at 10 UTC, (b) Jan 26, 2017, at 20 UTC, (c) Feb 3, 2023, at 10 UTC, and (d) Feb 3, 2023, at 20 UTC. Black dashed circles in panels (a) and (c) show the location of the main fire sectors. Black crosses indicate the sites used for the time series in Fig. 7.

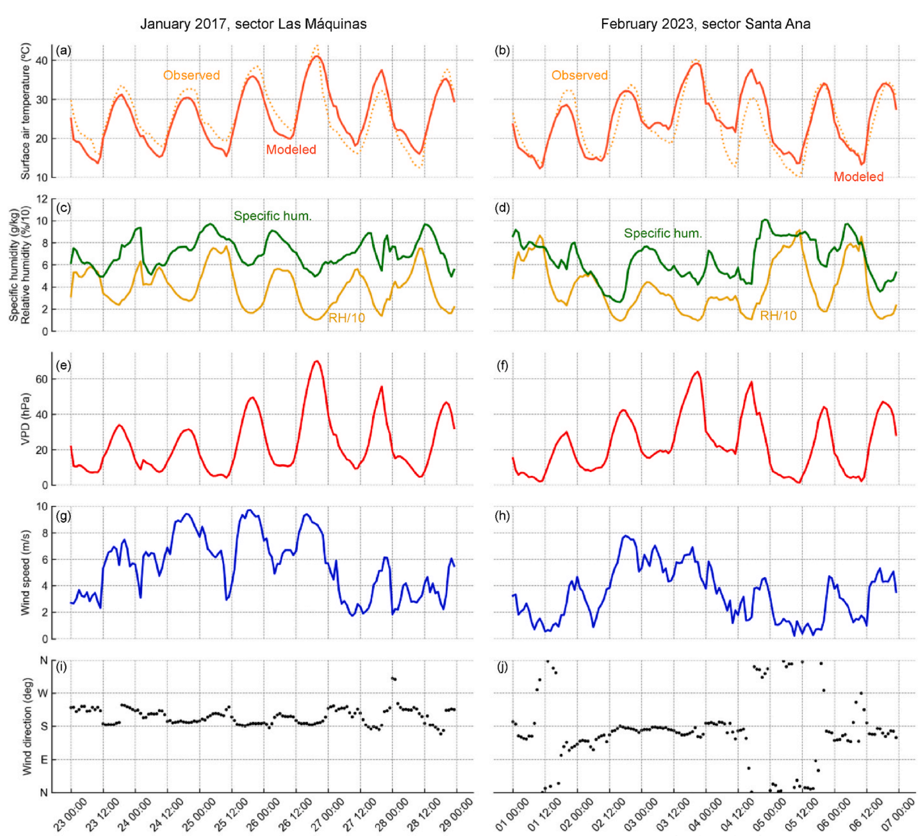

Fig. 7. Time series of main near-surface meteorological variables obtained from WRF simulations near the large fire sectors (black crosses in Fig. 6) during seven days around FO17 and FO23. Panels (a) and (b) include observed surface air temperature time series (dotted lines) from nearby weather stations.

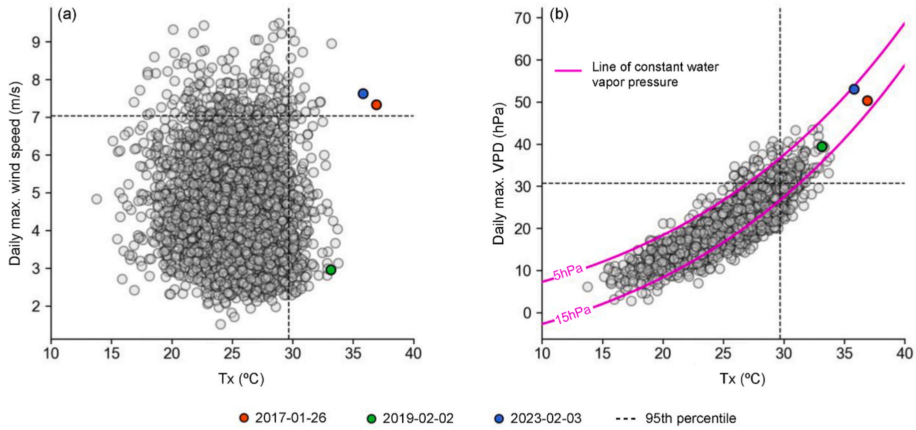

Fig. 8. (a) Scatter plot between daily maximum values of near-surface temperature (Tx) and wind speed obtained from 6-hourly ERA5 summer data (period 1979–2023). Tx values were obtained using the nearest grid point to General Bernardo O'Higgins (GBO) station, while wind speed values were calculated as the spatial average value over an area near the main fire sectors (Box 2 in Fig. 1). (b) The same as in (a) but for daily maximum vapor-pressure deficit (VPD) obtained from 1-hourly ERA5 summer data (period 1979–2023) at the nearest grid point to GBO. Fuchsia lines indicate curves of constant water vapor pressure.

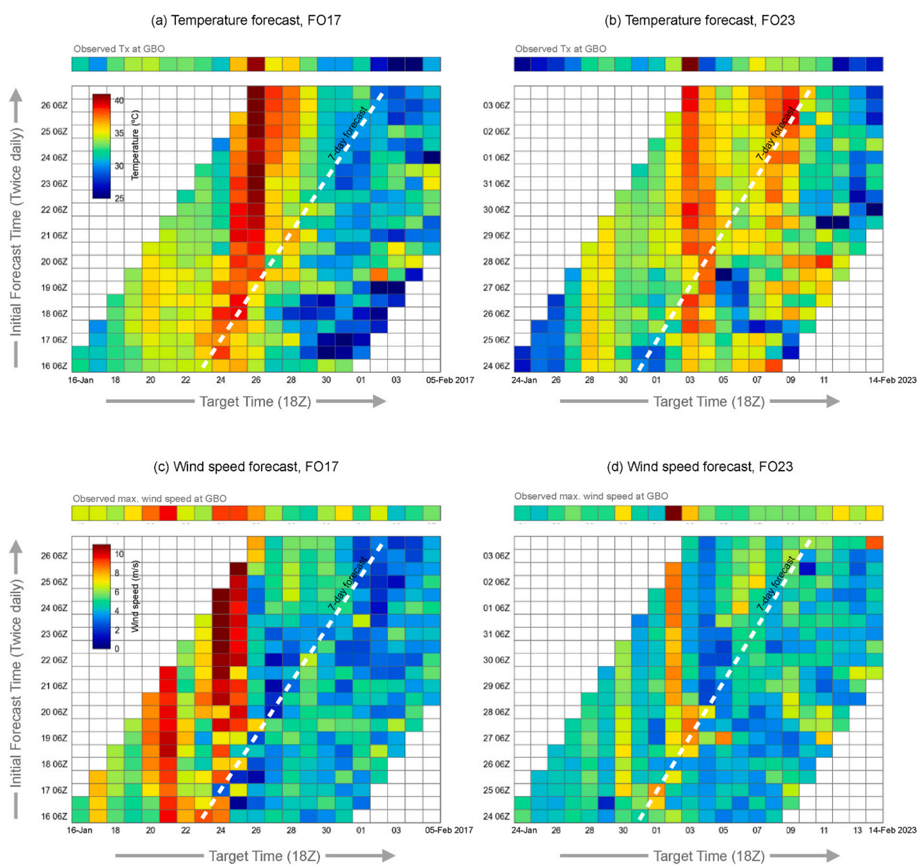

Fig. 9. Forecast of near-surface variables at 18 UTC for a grid point close to GBO station (36.5°S, 72°W) from the Global Forecast System (GFS). (a) 2-m air temperature (°C) for late January 2017. (b) The same as (a) but for early February 2023. (c) 10-m wind speed (m/s) for late January 2017. (d) The same as in (c) but for early February 2023. Each row corresponds to the forecast temperature for the next 15 days (one value per day, color-coded according to the scale in panels (a) and (c)) initialized at either 06Z or 18Z. The upper row shows the observed daily maximum values obtained from hourly data at GBO station. (For interpretation of the references to color in this figure legend, the reader is referred to the Web version of this article.)

In the first case -when 41.5 °C occurred on January 26, 2017-, the GFS began to predict extreme temperatures exceeding 38 °C by January 19 (initial time), about a week before the event (lead time). Subsequent initial times indicated 18 UTC air temperatures even closer to the observed value at the right time (Fig. 9a). A similar forecast evolution is evident for FO23 (Fig. 9b), with a prediction of the temperature peak on February 3, 2023 one week before, although the GFS value was about 2 °C lower than the observed value in this case.

Regarding wind speed, the GFS began to predict values similar to the one observed in FO17 one day earlier (Fig. 9c), and underestimated the wind speed observed in FO23 by nearly 3 m/s for almost all initial times (Fig. 9d). The GFS predicted extreme values during January 24–25, 2017 with a lead time of three days, capturing the timing of the wind maxima but overestimating the observed values by about 2 m/s.

Likewise, the GFS captured the timing of the wind maximum during early February 2023 with a lead time of three days, but underestimated the observed value by 3 m/s.

4.3. Synoptic and sub-synoptic scale conditions

The evolution of the Z500 and SLP fields for three days around FO17 and FO23 is shown in Fig. 10. In both cases, the mid-level circulation is characterized by a ridge drifting eastward from the extratropical southern Pacific. At the surface level, a low-pressure core is present along the central Chilean coast, accompanied by a surface anticyclone to the south, which is dynamically linked to the mid-level ridge and moves eastward across the Andes Cordillera. These features indicate the development of a *coastal low* that most often attends heat waves in central Chile (Garreaud et al., 2002; see Sect. 2.1).

The WRF simulations for January 26, 2017, and February 3, 2023 (Fig. 6), capture the low-level wind pattern that characterizes the coastal low, including strong southerlies along the coast to the south of the pressure minimum, broadly coincident with the latitude of the large fires, as well as intense easterly flow (Puelche wind; Montecinos et al., 2017) over the Andes of south-central Chile. During the afternoon of the fire outbreaks (Fig. 6b–d), a strong near-surface flow developed across the central valley and the coastal inland zones compared to the morning conditions (Fig. 6a–c). Although *southerly winds* prevailed in these zones, afternoon conditions further reveal that near the large fire sectors (SLM and SSA) a minor zonal component appeared, westerly in the case of FO17 and easterly in the case of FO23. To the north of the pressure minimum, relaxed northerlies start to develop in the afternoon hours, indicating the recovery of the surface pressure field.

The synoptic and sub-synoptic conditions associated with the coastal low development shown in Fig. 10 produced a strong low-tropospheric warming over south-central Chile, as revealed by the longitude-height cross-section of 24-hr warming constructed using the WRF outputs (Fig. 11a and b). Below the 850 hPa, the 24-hr warming reached values of 6 and 8 °C in the afternoons of FO17 and FO23, respectively. Crucial for this low-level warming is the marked subsidence in the free troposphere (Fig. 11c–f), which is synoptically driven ahead of the incoming ridge and topographically induced in the western slope of the Andes by the Puelche wind (Garreaud et al., 2002; Garreaud and Rutllant, 2003).

To quantify the extremity of the large-scale subsidence, we used ERA5 data from 1979 to 2023 every 6 h to construct empirical frequency distributions of the mid-level vertical velocity over the central valley at 36°S, 72°W. Fig. 12a shows such empirical distribution along with the most extreme values of ω_{500} for three days around FO17 and FO23. Both values are above the 99th percentile, although the mid-level subsidence was stronger in the January 2017 case. This difference is also evident in Fig. 11e and f, where the mid-level subsidence during FO17 is more marked than during FO23.

Despite the stronger free-troposphere subsidence in FO17, the lower-troposphere 24-hr warming that led to the extreme temperature was larger in FO23 (Fig. 11a and b). This could be explained by topographically induced subsidence driven by the Puelche wind (Fig. 11c and d). As before, we compare the maximum near-surface zonal wind (from ERA5) over the Andes (box 1 in Fig. 1) during FO17 and FO23 against the empirical frequency distribution of this variable on summer days. Noting that Puelche winds are associated with negative zonal flow, one can observe the extreme conditions in both events, being stronger in FO23 (Fig. 12b).

The role of the topographically-induced subsidence is further revealed by a numerical experiment using WRF in which the topography was reduced to 50% of its actual height. We ran these experiments and obtained a 24-h near-surface warming of about 4 °C in both cases

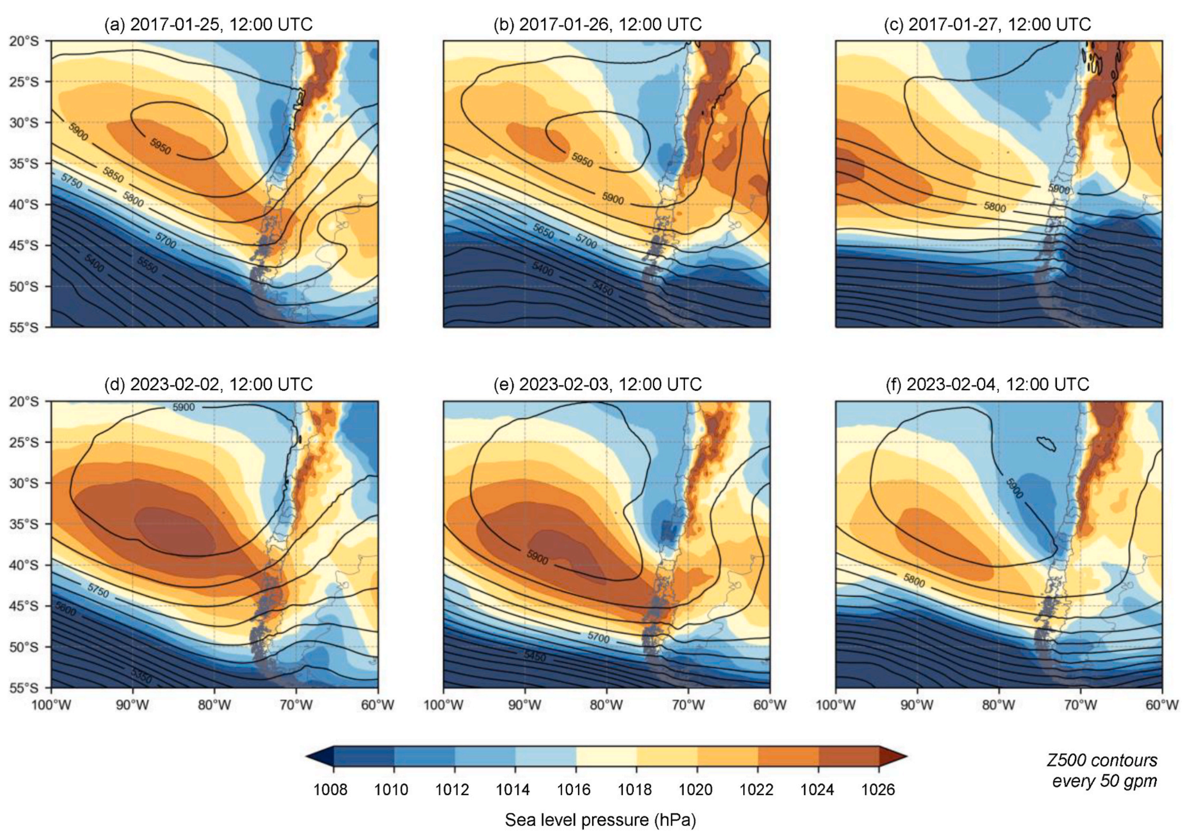

Fig. 10. Sea level pressure (colors in hPa) and geopotential height at 500 hPa (Z500, contours in geopotential meters (gpm)) during a three-day period around January 26, 2017 (panels a–c) and February 3, 2023 (panels d–f). All fields are at 12 UTC. (For interpretation of the references to color in this figure legend, the reader is referred to the Web version of this article.)

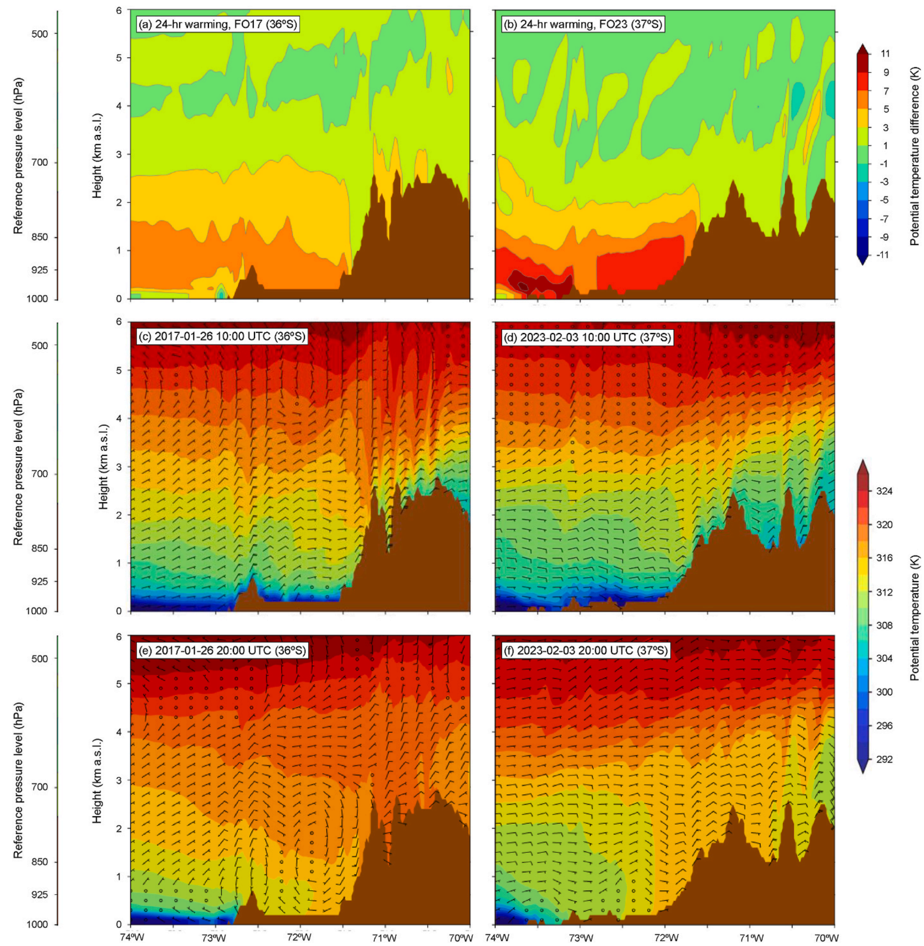

Fig. 11. (a) Longitude-height profile of the potential temperature difference between Jan 26, 2017 at 20 UTC and Jan 25, 2017 at 20 UTC (24-hr difference), based on WRF simulations. (b) The same as (a) but for a 24-hr difference ending on Feb 3, 2023 at 20 UTC. (c), (d), (e) and (f): Longitude-height profiles of potential temperature and vertical-zonal velocities based on WRF simulations. The nearest grid points to the specified latitudes were used, and the data were averaged over a 3-h period centered around the specified dates. Vertical velocity was scaled by a factor 50 and a gaussian filter was applied to zonal and vertical velocities before drawing the profiles. The topography is shown in brown filled contours. (For interpretation of the references to color in this figure legend, the reader is referred to the Web version of this article.)

(Fig. S4). Since the full-topography simulations have 24-h near-surface warming of 6 °C and 8 °C associated with FO17 and FO23, respectively, our results indicate a more significant role of the Puelche wind and its interaction with the Andes in the occurrence of FO23 than in that of FO17.

Although the Puelche wind was essential for the low-tropospheric and surface warming in both cases (Fig. 11c and d), it largely detached from the surface during the afternoon of FO23 at 37°S (Fig. 11f), and it is not present at the surface during the afternoon of FO17, when the mountain-valley circulation seems to dominate the wind pattern at the Andes foothills at 36°S (Fig. 11e). A Hovmöller diagram of potential temperature and horizontal wind near SLM (Fig. 13a) shows winds with easterly component of varying intensity in the layer 850-700 hPa from the morning of Jan 25, 2017, until the afternoon of Jan 26, 2017. Nonetheless, the wind below 925 hPa showed a westerly component during this period. A similar analysis near SSA (Fig. 13b) indicates that low-level winds with easterly components were present from the morning of Feb 2, 2023, until the morning of Feb 4, 2023. In this case, the near-surface winds also had an easterly component during the afternoon of FO23, although the prevailing direction was south. In both cases, the easterly component was more intense during the night before the events (00–12 UTC; 21-09HL), which suggests a more thermodynamic than the dynamic role of the Puelche winds in the occurrence of the fire outbreaks. In addition, the southeast direction of the low-level winds revealed by the Hovmöller diagrams allows us to explain the direction of the smoke plume produced by the fires during FO17 and FO23 (Fig. 1a and b).

4.4. Hemispheric-scale precursors

An analysis of upper-tropospheric stream function and Z500 anomalies during the three weeks before FO17 and FO23 reveals processes at scales larger than synoptic influencing the mid-level ridge and the low-level anticyclone mentioned above (Fig. 14). In the case of FO17, a mid-latitude anticyclonic anomaly persisted for at least three weeks in the low and mid-troposphere around 55°S, 140°W (Fig. 14a), from where downstream development towards South America enhanced the mid-level ridge over south-central Chile. As described by Demortier et al. (2021), at least two possible sources acted to sustain the anticyclonic anomaly over the South Pacific. First, a wave-train emanated from Western Australia, where deep convection also promoted a rainfall anomaly above 400% with respect to the 1961–1990 climatology. Second, anomalous tropical convection was observed during January 17–21 around 20°S, 140°W, consistent with an active Madden-Julian Oscillation (MJO) phase 1 (according to the Wheeler and Hendon index; Wheeler and Hendon, 2004), which possibly intensified the mid-latitude anticyclone (Demortier et al., 2021).

The synoptic and surface weather conditions around FO23 occurred

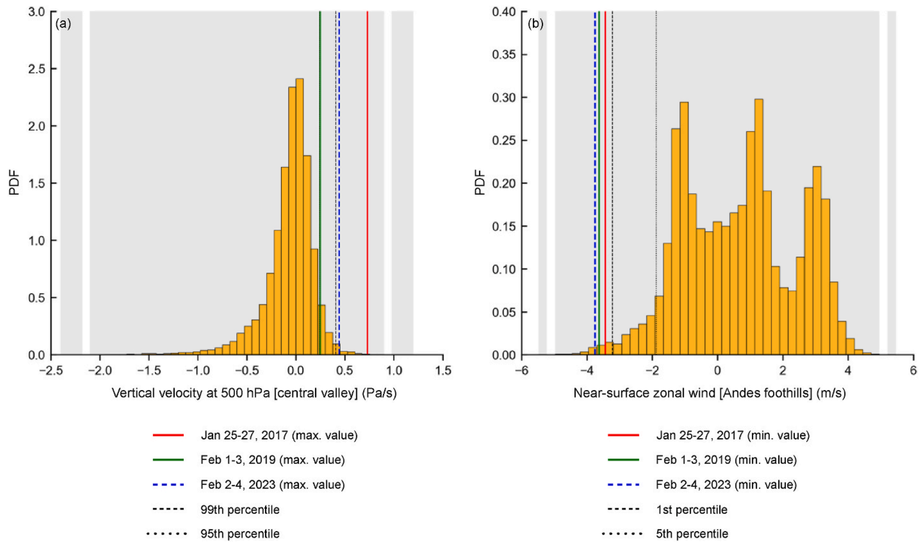

Fig. 12. (a) Empirical frequency distribution of 6-hourly mid-level vertical velocity (Pa/s) at 36°S, 72°W during summer according to ERA5 data from 1979 to 2023. Vertical lines in red, green and blue indicate the maximum value in a three-day period around Jan 26, 2017, Feb 2, 2019 and Feb 3, 2023, respectively. Dotted and dashed black lines correspond to the 95th and 99th percentile, respectively. (b) Histogram as in (a) but for minimum zonal wind averaged over Box 1 (38-36.5°S, 71.7–71.5°W; B1 in Fig. 1c). Vertical lines in red, green and blue indicate the minimum value in a three-day period around Jan 26, 2017, Feb 3, 2019 and Feb 3, 2023, respectively. Dotted and dashed black lines correspond to the 5th and 1st percentile, respectively. Bins containing data are displayed with a gray background for better visibility. (For interpretation of the references to color in this figure legend, the reader is referred to the Web version of this article.)

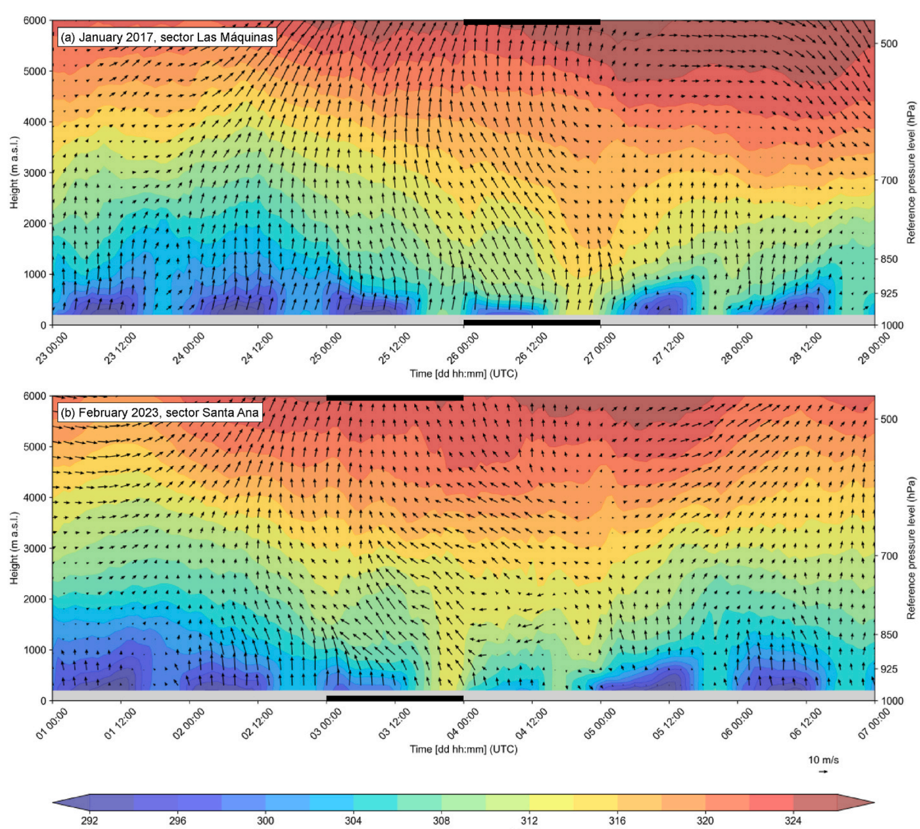

Fig. 13. (a) Hovmöller diagrams of potential temperature and horizontal wind near Sector Las Máquinas (black cross in Fig. 6a) during a 7-day period around FO17. (b) The same as (a) but for a point near Sector Santa Ana (black cross in Fig. 6c) during a 7-day period around FO23. The thick black lines indicate the time period spanning from the night before the fire outbreaks until the afternoon during the events.

in the context of the intraseasonal evolution of a wave train over the South Pacific that influenced a mid-level ridge over south-central Chile (Fig. 14b). In this case, the source of the intraseasonal activity seems linked to the presence of a mid-level geopotential height dipole over the southwest Indian Ocean approximately two weeks before the event (Fig. 14b). This pattern has been previously identified as a precursor of heatwaves in central Chile (Jacques-Coper et al., 2021). Additionally, the MJO remained active on phase 3 during January 20–31 and

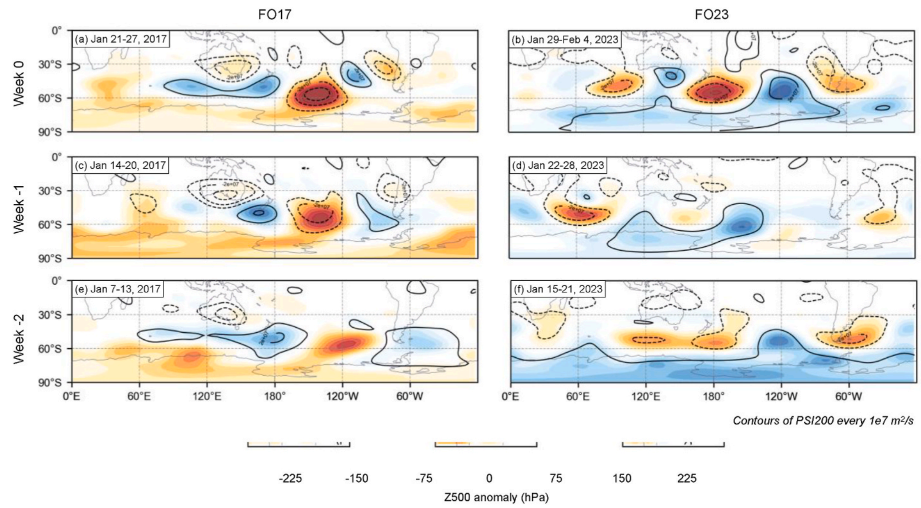

Fig. 14. Hemispheric-scale precursors of FO17 and FO23. (a) Composites of geopotential height at 500 hPa (Z500, colors in hPa) and 0.2101 sigma streamfunction (PSI200, contours every 1e7 m^2/s) anomalies (with respect to 1991–2020 climatology) computed from the NCEP-NCAR Reanalysis 1 for a 7-day period including FO17. (c) and (e) The same as (a) but for one and two weeks before the 7-day period including FO17, respectively. (b), (d) and (f) The same as (a), (c) and (e) but for FO23. (For interpretation of the references to color in this figure legend, the reader is referred to the Web version of this article.)

transitioned to active phase 4 until FO23. This situation depicts deep convection extending from the tropical Indian Ocean towards the Maritime Continent, which apparently acted as a further wave train source.

4.5. The role of climate change on extreme temperatures

South-central Chile has featured significant summer warming trends during the last few decades (González-Reyes et al., 2023). For example, at General Bernardo O'Higgins, time series of the mean and 95th-percentile summer Tx show positive linear trends of 0.36 and 0.47 °C/decade in the period 1970–2023, respectively (both trends are statistically significant at a 5% level; Fig. 5a). On the other hand, the wind speed near the main fire sectors has remained relatively stable over the last decades. According to ERA5 data, time series of mean and 95th-percentile daily maximum wind speed near the coastal zone (Box 2 in Fig. 1) show non-significant linear trends (at 5% of statistical significance) in the period 1980–2023 (Fig. S5). Given the increasing temperatures in the study area, in this section, we employ a probability-based method for EEA (see Sect. 2.3 for details) to explore the possible influence of climate change on extreme temperatures in south-central Chile, particularly on those observed during FO17 and FO23. We opt not to conduct a similar analysis for wind speed due to the lack of significant trends.

We define our variable of interest as the highest near-surface temperature reached during summer in south-central Chile (xTx; Fig. 5a) and characterize the extreme temperatures during FO17 and FO23 as warm events surpassing the threshold value of 42 °C. The selection of the variable of interest and threshold value allows us to increase the extremity of events in accordance with EEA recommendations (e.g., Cattiaux and Ribes, 2018), as warm events during FO17 and FO23 are the only instances above the selected threshold in the historical record (Fig. 5a), and we are not concerned with the specific location or timing of these warm events. Consequently, we investigate the changes in the probability and intensity of summer warm events above 42 °C in south-central Chile due to climate change.

We use the CESM-LE to fit the statistical model from Sect. 2.3 and assess changes in extremes. This ensemble had been previously validated for mean statistics and subjected to bias correction (refer to Sect. 2.2 for details). To validate the representation of extremes in the CESM-LE, we compare the ensemble-based estimates with the parameter estimates derived from fitting the CR2Met xTx (Fig. S6). Overall, the CESM-LE shows a good performance in accurately representing temperature extremes in south-central Chile.

For warm events exceeding 42 °C, we obtain a present-day return period of about 220 yr (95% CI: [192, 265] yr; Fig. 15). When comparing preindustrial and present-day climates, we estimate that the warm events under examination have intensified by 1.3 °C (95% CI: [1.2, 1.3] °C), and their probability has increased by nearly 20 times (95% CI: [19, 24]) due to climate change. Similarly, we estimate that events similar to those studied will experience an increase in intensity of 1.0 °C (95% CI: [1.0, 1.0] °C) and an increase in probability by seven times (95% CI: [6, 7]) in a future climate that is 2 °C above preindustrial levels, as a result of climate change (as compared to the present-day climate).

5. Discussion

This study identified extreme surface weather conditions during FO17 and FO23, thereby complementing and expanding previous works on these events (Bowman et al., 2019; Cordero et al., 2024) and active fire months (McWethy et al., 2021). In particular, we found that maximum temperatures across south-central Chile (Tx > 41 °C) were well above the previous records during these days, resulting in the highest-ever observed VPD values during the fire outbreaks. Likewise, we show that surface wind speed near the main fire sectors exceeded the 95th percentile of the historical distribution, implying the occurrence of extreme compound weather events during the fire outbreaks. We hypothesize that these conditions exacerbated the expansion of the wildfires during FO17 and FO23, contributing significantly to the daily burned area values observed in the region.

In addition, our results showed that numerical weather forecasts are capable of anticipating extreme temperature conditions. These findings are preliminary but promising, as the direct model outputs were able to predict the timing and extremity of the maximum temperature during FO17 and FO23 and there were no false alarms. The proper prediction of high air temperature further implies high VPD given the tight relationship between both variables (Fig. 8b). Additionally, the wind speed during FO17 was accurately predicted by the forecast, and the timing of the extreme wind conditions previous to FO17 and FO23 was properly captured. Thus, our results suggest that, to a great extent, direct outputs from numerical weather forecasts could effectively predict future extreme fire weather events in the study area. Therefore, a more comprehensive analysis of the predictability of these extreme events is warranted, considering data across the whole domain, other variables, and full summer seasons.

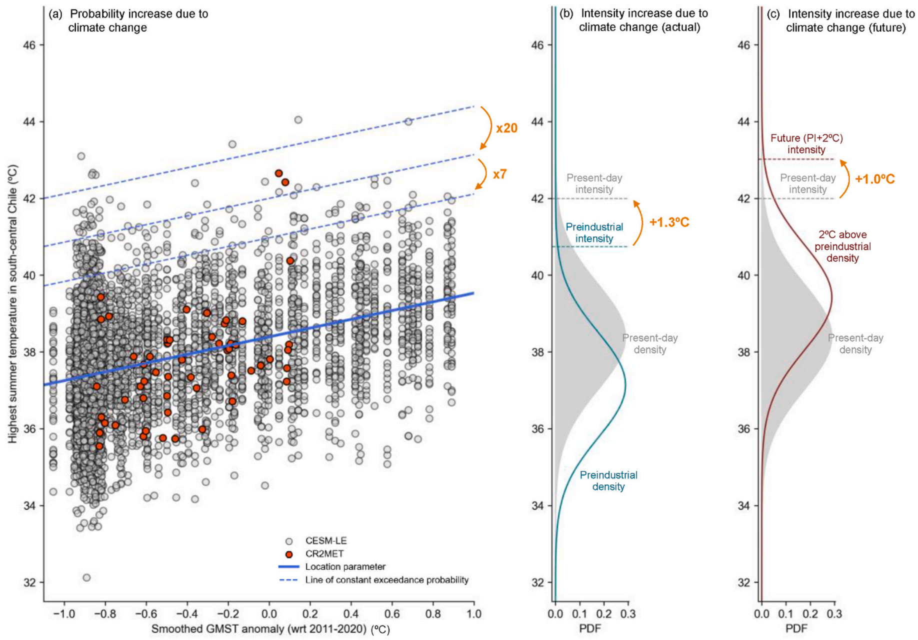

Fig. 15. Changes in extreme temperature behavior due to climate change in south-central Chile. (a) Scatter plot between highest summer temperature in south-central Chile (xTx) and the smoothed GMST anomaly (with respect to 2011–2020). The gray circles represent xTx values from the CESM-LE simulation, and red circles indicate the values obtained from the CR2Met dataset. The solid blue line corresponds to the location parameter of a GMST-dependent normal distribution fitted to the CESM-LE xTx values. Dashed blue lines represent lines of constant exceedance probability according to the CESM-LE, showing that a 42 °C event would be 20 times less probable in the preindustrial (PI) climate (GMST anomaly of −1.1 °C) and 7 times more probable in a future climate 2 °C warmer than PI levels (PI+2 °C; GMST anomaly of 0.9 °C). (b) Present-day and PI distributions of xTx according to CESM-LE. Extreme warm events of return period similar to FO17 and FO23 have increased their intensity by 1.3 °C due to climate change in comparison to PI intensity. (c) The same as in (b) but for future (PI+2 °C) and present-day climates, showing a 1.0 °C intensity increase of events of return period similar to FO17 and FO23 due to climate change. (For interpretation of the references to color in this figure legend, the reader is referred to the Web version of this article.)

An intricate question arising from our results is whether temperature and wind contributed equally to the occurrence of fire outbreaks. As described in Sect. 4.2, temperature (and VPD) maxima occurred concurrent to the fire outbreaks, whereas the wind speed maxima (relative to the seven-day simulation period) occurred one day before the fire outbreaks. Since SLM and SSA were already burning when the wind speed maxima occurred (e.g., the Las Máquinas fire complex began seven days before FO17), our results suggest that the unprecedented high temperatures triggered the necessary conditions for the observed fire spread rates. Likely, these conditions consisted in low contents of fuel moisture, favoring fuel consumption, fire spread, and fire intensity (e.g., Srock et al., 2018). High rates of fuel drying possibly occurred before the fire outbreaks (e.g., during the wind speed maxima), but the fuel moisture contents remained too high to produce extreme fire spread rates. Instead, the fuel drying rates driven by the temperature maxima likely reduced the fuel moisture enough to cause the fire spread observed during FO17 and FO23.

Our study also clarifies the role of the downslope flow during these events. Easterly winds (Puelche) blowing down the western slope of the Andes enhance subsidence and contribute to warm and dry conditions over the central valley (e.g., Rutllant and Garreaud, 2004; González-Reyes et al., 2023). Nonetheless, strong near-surface *southerly* winds, rather than easterly winds, were observed in the main fire sectors before and during FO17 and FO23 (Figs. 6 and 7). At these locations, the easterly winds were mostly detached from the surface (Fig. 13), and the near-surface winds were primarily driven by the synoptically-induced pressure gradient. Thus, the Puelche wind contributed to the fire spread conditions by warming and drying the lower atmosphere. Moreover, it is likely that the Puelche wind was indispensable for the extremely warm and dry conditions observed during FO17 and FO23, as it is a crucial factor for the occurrence of upper-quantile temperatures in GBO (Fig. S7a). On the other hand, Puelche wind over the Andes and southerly winds near the coast of south-central Chile exhibit no statistically significant correlation on a daily scale (Fig. S7b). Intense Puelche wind events leading to upper-quantile values of temperature and VPD at GBO can be associated with weak winds where most exotic plantations are concentrated. This situation effectively occurred during the summer of 2019 (green line in Fig. 5b and green circles in Fig. 8), possibly explaining the non-extreme burned area values recorded during the 2018/19 fire season (Fig. 2).

Although we did not address the role of seasonal anomalies in the occurrence of extreme fire seasons in the region, we acknowledge their potential influence on fuel load and fuel moisture. Indeed, the coastal Maule region had a precipitation surplus of ~20% during the winter of 2015 (i.e., the winter preceding the start of the 2016/17 fire season) likely favoring vegetation growth in a sector more dominated by a fuel-limited fire regime (González and Veblen, 2006; González et al., 2011; Holz et al., 2012, 2017; Urrutia-Jalabert et al., 2018). On the other hand, the coastal Biobio region had a precipitation deficit of ~40% and a mean Tx anomaly of 1.8 °C between November 2022 and January 2023 (i.e., spring and summer concurrent with the 2022/2023 fire season), likely contributing to fuel drying in a sector characterized by a climate-limited fire regime (Holz et al., 2012; Urrutia-Jalabert et al., 2018; McWethy et al., 2021). Therefore, the seasonal anomalies of the relevant meteorological variables favored the occurrence of large burned areas during the extreme fire seasons in south-central Chile.

Climate change also has conditioned the occurrence of extreme fire seasons in south-central Chile affecting processes across various scales of variability. It has significantly contributed to the long-term drying and warming trend exhibited inland in the region during the last sixty years (Falvey and Garreaud, 2009; Boisier et al., 2016, 2018). These processes have likely favored the long-term drying of flammable vegetation, thus promoting fire spread conditions, especially in zones where moisture availability modulates fire activity (i.e., climate-limited regime;

González et al., 2011; Cordero et al., 2024). Additionally, since 2010, the region has undergone an extended period of drought, the so-called megadrought, which has been partially attributed to climate change (Garreaud et al., 2017, 2020; Boisier et al., 2018) and has also been associated with an enhancement of fire activity (González et al., 2018). Regarding the short-term scale, the present study has formally attributed the recent extreme warm events observed in the region to climate change, demonstrating that the likelihood and intensity of such warm events have increased due to climate change.

Our results represent a novel contribution to understanding climate change's impacts on fire activity in the region since they expand the characterization of different scales at which climate change has affected fire-related atmospheric phenomena in the region, which ranges from short-term (i.e., extreme weather) to mid-term (i.e., megadrought) to long-term scales of variability (i.e., drying and warming trends). Furthermore, our results reveal the future contribution of climate change on weather conditions favorable to the occurrence of extreme fire outbreaks, in agreement with previous studies on the topic (McWethy et al., 2021; Rapanague, 2022; Cordero et al., 2024). Future investigations could explore different statistical models to represent extreme behavior beyond relying solely on a linear dependence on GMST. Additionally, utilizing multiple global climate models can help assess model uncertainty, an important aspect of attribution assessment that falls beyond the scope of the current work. To develop a complete picture of the role of climate change in weather conditions favoring extreme fire outbreaks, additional studies will be needed that explore the impacts of climate change on wind patterns (e.g., Puelche wind) and the underlying mechanisms by which anthropogenic forcing affects extremely behavior in the region.

The occurrence, extent, and behavior of these extreme wildfires result from a complex interplay of climatic and non-climatic variables (Bowman et al., 2011; Abatzoglou et al., 2021). In addition to climate, other factors such as topography, human presence and vegetation are all relevant to explain fire occurrence and spread (McWethy et al., 2018). For example, in south-central Chile, non-native plantations (mainly *Pinus radiata* and *Eucalyptus* spp) are the predominant vegetation type burnt during large fires (González et al., 2020), since fuels in these ecosystems have higher flammability, may accumulate in higher quantities, and present higher vertical and horizontal continuity at multiple scales (i.e., stands to landscapes) (Pauchard et al., 2008; Cóbar-Carranza et al., 2015). During late January 2017, the predominant vegetation types burnt were non-native plantations (43%) and grass/shrub rangelands (44%), followed by native forest (11%) (Bowman et al., 2019), while during early February 2023, they were non-native plantations (over 60%), followed by native forests (c.a. 20%) and grass/shrub rangelands (13%) (Rafael Garcia pers. comm.). In both cases, non-native plantations represented a significant fraction of the area consumed by the fires, likely playing a major role in the fire spread due to their higher susceptibility to fire.

In addition, a fundamental component that has been the focus of many controversies is the causes of the ignitions in both fire outbreaks. Although lightning-ignited fires are common in other parts of the world, lightning during the summer season in south-central Chile is mainly confined to high elevations over the Andes in the Araucanía administrative region (Francisco Gómez pers. comms.), far from the large fire sectors. Furthermore, clear-sky conditions prevailed during the fire outbreaks (Fig. 1a and b), and no convective storms were reported or indicated by the WRF simulations before the fire outbreaks, implying that the fires were directly caused by human activities either accidently (e.g., escapes from rural controlled-burns, machineries, power line sparks) or intentionally (arson). Further research is needed to determine how much multiple ignition events contributed to increase the total burned area during FO17 and FO23. Quantifying the relative contribution of climatic and non-climatic factors in the unprecedently large burned area values during these fire outbreaks calls for numerical experiments with fire models in which the meteorological forcing and other variables can be altered. Future work could integrate advanced fire behavior models within WRF simulations to better represent the interactive processes between wildfires and the atmosphere, and to assess the contribution of non-climatic factors in such events (e.g., Coen et al., 2013; Kartsios et al., 2021; Turney et al., 2023).

6. Conclusions

The largest burned areas in south-central Chile were recorded during the 2016/17 and 2022/23 fire seasons, which were about ten times larger than the historical average, resulting in significant socio-environmental impacts. The purpose of the current study was to provide a comprehensive analysis of the meteorological conditions during the extreme fire events in late January 2017 and early February 2023 that largely explain these seasonal-aggregated values, ranging from local to global phenomena. We found that extraordinary daily burned area values (>65,000 ha) occurred under extreme weather conditions, with temperature, VPD, and wind speed values during these days exceeding by far the 95th percentile of the historical distribution. In particular, VPD and daytime temperatures during FO17 and FO23 established new records. Based on these results, we hypothesize that extreme meteorological conditions played a crucial role in the occurrence of the fire outbreaks under study and, consequently, in the corresponding fire seasons.

Our findings further reveal that these local conditions resulted from intense coastal southerly winds and large-scale subsidence enhanced by easterly downslope winds (Puelche) near the Andes foothills. These elements were orchestrated by an eastward drifting of a mid-level ridge and the development of a surface low along the subtropical west coast of South America. Hemispheric-scale precursors of these extreme weather events were also identified in both cases. Additionally, we demonstrated that climate change has played an essential role in increasing the present (and future) probability and intensity of extreme warm temperatures like those observed during the fire outbreaks. Along with extreme weather conditions, other climatic and non-climatic factors (e.g., prolonged drought, long-term trends, fuel availability, LUCC, and human ignitions) likely contributed to extraordinarily large burned area values during late January 2017 and early February 2023. Future modeling efforts considering fire behavior could help quantify the relative contribution of these causal factors in the extreme fire activity in the region. We note, however, that non-climatic factors have remained relatively stable in the last decade, pointing to a more prominent role of the occurrence of unprecedented, extreme weather in setting the stage for similarly unprecedented fire activity in Chile. Unfortunately, severe forest-fire weather conditions are expected to be more recurrent under climate change scenarios.

Funding

This research has been supported by the Center for Climate and Resilience Research (ANID/FONDAP/1523A0002). AP was funded by ANID/BASAL FB210006.

Code availability

The software used in this study is available upon request to the corresponding author.

CRediT authorship contribution statement

Tomás Carrasco-Escaff: Writing – original draft, Visualization, Software, Methodology, Investigation, Formal analysis, Conceptualization. **René Garreaud:** Writing – original draft, Visualization, Supervision, Formal analysis, Conceptualization. **Deniz Bozkurt:** Writing – review & editing, Visualization, Investigation, Formal analysis, Conceptualization. **Martín Jacques-Coper:** Writing – review & editing, Formal analysis, Conceptualization. **Aníbal Pauchard:** Writing – review & editing, Conceptualization.

Declaration of competing interest

The authors declare that they have no known competing financial interests or personal relationships that could have appeared to influence the work reported in this paper.

Data availability

Data will be made available on request.

Acknowledgements

We would like to thank the Center for Climate and Resilience Research for supporting us with data and equipment to carry out this work. Additionally, we would like to thank Rafael García for providing the data on the types of vegetation burned during the fire outbreaks, and two anonymous referees for their constructive and useful comments and recommendations. Powered@NLHPC: This research/thesis was partially supported by the supercomputing infrastructure of the NLHPC (CCSS210001).

Appendix A. Supplementary data

Supplementary data to this article can be found online at https://doi.org/10.1016/j.wace.2024.100716.

References

Abatzoglou, J.T., Williams, A.P., 2016. Impact of anthropogenic climate change on wildfire across western US forests. Proc. Natl. Acad. Sci. USA 113 (42), 11770–11775.

Abatzoglou, J.T., Juang, C.S., Williams, A.P., Kolden, C.A., Westerling, A.L., 2021. Increasing synchronous fire danger in forests of the western United States. Geophys. Res. Lett. 48, e2020GL091377 https://doi.org/10.1029/2020GL091377.

Alvarez-Garreton, C., Mendoza, P.A., Boisier, J.P., Addor, N., Galleguillos, M., Zambrano-Bigiarini, M., et al., 2018. The CAMELS-CL dataset: catchment attributes and meteorology for large sample studies–Chile dataset. Hydrol. Earth Syst. Sci. 22 (11), 5817–5846.

Arévalo, J., Marín, J.C., Díaz, M., Raga, G., Pozo, D., Córdova, A.M., Baumgardner, D., 2023. Sensitivity of simulated conditions to different parameterization choices over complex terrain in Central Chile. Atmosphere 15 (1), 10.

Boisier, J.P., Rondanelli, R., Garreaud, R.D., Muñoz, F., 2016. Anthropogenic and natural contributions to the Southeast Pacific precipitation decline and recent megadrought in central Chile. Geophys. Res. Lett. 43 (1), 413–421.

Boisier, J.P., Alvarez-Garreton, C., Cordero, R.R., Damiani, A., Gallardo, L., Garreaud, R. D., et al., 2018. Anthropogenic drying in central-southern Chile evidenced by long-term observations and climate model simulations. Elem Sci Anth 6, 74.

Bowman, D.M., Balch, J.K., Artaxo, P., Bond, W.J., Carlson, J.M., Cochrane, M.A., et al., 2009. Fire in the Earth system. Science 324 (5926), 481–484.

Bowman, D.M., Balch, J., Artaxo, P., Bond, W.J., Cochrane, M.A., D'antonio, C.M., et al., 2011. The human dimension of fire regimes on Earth. J. Biogeogr. 38 (12), 2223–2236.

Bowman, D.M., Moreira-Muñoz, A., Kolden, C.A., Chávez, R.O., Muñoz, A.A., Salinas, F., et al., 2019. Human–environmental drivers and impacts of the globally extreme 2017 Chilean fires. Ambio 48, 350–362.

Bowman, D.M., Kolden, C.A., Abatzoglou, J.T., Johnston, F.H., van der Werf, G.R., Flannigan, M., 2020. Vegetation fires in the anthropocene. Nat. Rev. Earth Environ. 1 (10), 500–515.

Campos, C., Couto, F.T., Santos, F.L., Rio, J., Ferreira, T., Salgado, R., 2024. ECMWF lightning forecast in mainland Portugal during four fire seasons. Atmosphere 15 (2), 156.

Carmona, A., González, M., Nahuelhual, L., Silva, J., 2012. Spatio-temporal effects of human drivers on fire danger in Mediterranean Chile. Revista Bosque 33 (3), 321–328.

Cleveland, W.S., 1979. Robust locally weighted regression and smoothing scatterplots. J. Am. Stat. Assoc. 74 (368), 829–836.

Cóbar-Carranza, A.J., García, R.A., Pauchard, A., Peña, E., 2015. Efecto de la alta temperatura en la germinación y supervivencia de semillas de la especie invasora Pinus contorta y dos especies nativas del sur de Chile. Bosque 36 (1), 53–60.

Coen, J.L., Cameron, M., Michalakes, J., Patton, E.G., Riggan, P.J., Yedinak, K.M., 2013. WRF-Fire: coupled weather–wildland fire modeling with the weather research and forecasting model. J. Appl. Meteorol. Climatol. 52 (1), 16–38.

CONAF, 2023. Estadísticas históricas. from. https://www.conaf.cl/incendios-forestales/incendios-forestales-en-chile/estadisticas-historicas/. (Accessed 12 December 2023) [In Spanish].

Cordero, R.R., Feron, S., Damiani, A., Carrasco, J., Karas, C., Wang, C., et al., 2024. Extreme fire weather in Chile driven by climate change and El Niño–Southern Oscillation (ENSO). Sci. Rep. 14 (1), 1974.

Demortier, A., Bozkurt, D., Jacques-Coper, M., 2021. Identifying key driving mechanisms of heat waves in central Chile. Clim Dyn. https://doi.org/10.1007/s00382-021-05810-z (in press).

Díaz-Hormazábal, I., González, M.E., 2016. Spatio-temporal analyses of wildfires in the region of Maule, Chile. Revista Bosque 37 (1), 147–158.

Duane, A., Castellnou, M., Brotons, L., 2021. Towards a comprehensive look at global drivers of novel extreme wildfire events. Climatic Change 165 (3), 43.

Dudhia, J., 1989. Numerical study of convection observed during the winter monsoon experiment using a mesoscale two-dimensional model. J. Atmos. Sci. 46 (20), 3077–3107. https://doi.org/10.1175/1520-0469(1989)046<3077:NSOCOD>2.0.CO;2.

Echeverría, C., Coomes, D., Salas, J., Rey-Benayas, J.M., Lara, A., Newton, A., 2006. Rapid deforestation and fragmentation of Chilean temperate forests. Biol. Conserv. 130 (4), 481–494.

Ellis, T.M., Bowman, D.M., Jain, P., Flannigan, M.D., Williamson, G.J., 2022. Global increase in wildfire risk due to climate-driven declines in fuel moisture. Global Change Biol. 28 (4), 1544–1559.

Falvey, M., Garreaud, R.D., 2009. Regional cooling in a warming world: recent temperature trends in the southeast Pacific and along the west coast of subtropical South America (1979–2006). J. Geophys. Res. Atmos. 114 (D4).

Feron, S., Cordero, R.R., Damiani, A., Llanillo, P.J., Jorquera, J., Sepulveda, E., Asencio, V., Laroze, D., Labbe, F., Carrasco, J., Torres, G., 2019. Observations and projections of heat waves in South America. Sci. Rep. 9, 8173. https://doi.org/10.1038/s41598-019-44614-4.

Garreaud, R., Rutllant, J., 2003. Coastal lows along the subtropical west coast of South America: numerical simulation of a typical case. Mon. Weather Rev. 131 (5), 891–908.

Garreaud, R., Rutllant, J., Fuenzalida, H., 2002. Coastal lows along the subtropical west coast of South America: mean structure and evolution. Mon. Weather Rev. 130 (1), 75–88. https://doi.org/10.1175/1520-0493(2002)130<0075:CLATSW>2.0.CO;2.

Garreaud, R.D., Alvarez-Garreton, C., Barichivich, J., Boisier, J.P., Christie, D., Galleguillos, M., et al., 2017. The 2010–2015 megadrought in central Chile: impacts on regional hydroclimate and vegetation. Hydrol. Earth Syst. Sci. 21 (12), 6307–6327.

Garreaud, R.D., Boisier, J.P., Rondanelli, R., Montecinos, A., Sepúlveda, H.H., Veloso-Aguila, D., 2020. The central Chile mega drought (2010–2018): a climate dynamics perspective. Int. J. Climatol. 40 (1), 421–439.

Giannaros, T.M., Papavasileiou, G., Lagouvardos, K., Kotroni, V., Dafis, S., Karagiannidis, A., Dragozi, E., 2022. Meteorological analysis of the 2021 extreme wildfires in Greece: lessons learned and implications for early warning of the potential for pyroconvection. Atmosphere 13 (3), 475.

Giglio, L., Justice, C., Boschetti, L., Roy, D., 2021. MODIS/Terra+Aqua burned area monthly L3 global 500m SIN grid V061. In: NASA EOSDIS Land Processes Distributed Active Archive Center, 2023-06-01 from. https://doi.org/10.5067/MODIS/MCD64A1.061.

González, M.E., Veblen, T.T., 2006. Climatic influences on fire in Araucaria araucana–Nothofagus forests in the Andean cordillera of south-central Chile. Ecoscience 13 (3), 342–350.

González, M.E., Lara, A., Urrutia, R., Bosnich, J., 2011. Cambio climático y su impacto potencial en la ocurrencia de incendios forestales en la zona centro-sur de Chile (33°-42° S). Bosque 32 (3), 215–219.

González, M.E., Gómez-González, S., Lara, A., Garreaud, R., Díaz-Hormazábal, I., 2018. The 2010–2015 Megadrought and its influence on the fire regime in central and south-central Chile. Ecosphere 9 (8), e02300.

González, M.E., Sapiains, R., Gómez-González, S., Garreaud, R., Miranda, A., Galleguillos, M., et al., 2020. Incendios forestales en Chile: causas, impactos y resiliencia. Centro de Ciencia del Clima y la Resiliencia (CR) 2, 84.

González-Reyes, Á., Jacques-Coper, M., Bravo, C., Rojas, M., Garreaud, R., 2023. Evolution of heatwaves in Chile since 1980. Weather Clim. Extrem. 41, 100588 https://doi.org/10.1016/j.wace.2023.100588.

Grell, G.A., Dévényi, D., 2002. A generalized approach to parameterizing convection combining ensemble and data assimilation techniques. Geophys. Res. Lett. 29 (14), 38. https://doi.org/10.1029/2002GL015311, 1.

Grillakis, M., Voulgarakis, A., Rovithakis, A., Seiradakis, K.D., Koutroulis, A., Field, R.D., et al., 2022. Climate drivers of global wildfire burned area. Environ. Res. Lett. 17 (4), 045021.

Hansen, J., Ruedy, R., Sato, M., Lo, K., 2010. Global surface temperature change. Rev. Geophys. 48 (4).

Hersbach, H., Bell, B., Berrisford, P., Hirahara, S., Horányi, A., Muñoz-Sabater, J., et al., 2020. The ERA5 global reanalysis. Q. J. R. Meteorol. Soc. 146 (730), 1999–2049.

Holz, A., Kitzberger, T., Paritsis, J., Veblen, T.T., 2012. Ecological and climatic controls of modern wildfire activity patterns across southwestern South America. Ecosphere 3 (11), 1–25.

Holz, A., Paritsis, J., Mundo, I.A., Veblen, T.T., Kitzberger, T., Williamson, G.J., et al., 2017. Southern Annular Mode drives multicentury wildfire activity in southern South America. Proc. Natl. Acad. Sci. USA 114 (36), 9552–9557.

Instituto Nacional de Estadísticas, 2023. Censo de Población y Vivienda. from. https://www.ine.gob.cl/estadisticas/sociales/censos-de-poblacion-y-vivienda/censo-de-poblacion-y-vivienda. (Accessed 9 December 2023) [In Spanish].

Jacques-Coper, M., Veloso-Aguila, D., Segura, C., Valencia, A., 2021. Intraseasonal teleconnections leading to heat waves in central Chile. Int. J. Climatol. 41 (9), 4712–4731.
Kalnay, E., Kanamitsu, M., Kistler, R., Collins, W., Deaven, D., Gandin, L., Iredell, M., Saha, S., White, G., Woollen, J., Zhu, Y., Chelliah, M., Ebisuzaki, W., Higgins, W., Janowiak, J., Mo, K.C., Ropelewski, C., Wang, J., Leetmaa, A., Reynolds, R., Jenne, R., Joseph, D., 1996. The NCEP/NCAR 40-year reanalysis project. Bull. Am. Meteorol. Soc. 77 (3), 437–472. https://doi.org/10.1175/1520-0477(1996)077<0437:TNYRP>2.0.CO;2.
Kartsios, S., Karacostas, T., Pytharoulis, I., Dimitrakopoulos, A.P., 2021. Numerical investigation of atmosphere-fire interactions during high-impact wildland fire events in Greece. Atmos. Res. 247, 105253.
Kay, J.E., Deser, C., Phillips, A., Mai, A., Hannay, C., Strand, G., et al., 2015. The Community Earth System Model (CESM) large ensemble project: a community resource for studying climate change in the presence of internal climate variability. Bull. Am. Meteorol. Soc. 96 (8), 1333–1349.
Kelly, L.T., Giljohann, K.M., Duane, A., Aquilué, N., Archibald, S., Batllori, E., et al., 2020. Fire and biodiversity in the anthropocene. Science 370 (6519), eabb0355.
Kharin, V.V., Zwiers, F.W., 2005. Estimating extremes in transient climate change simulations. J. Clim. 18 (8), 1156–1173.
Kochi, I., Donovan, G.H., Champ, P.A., Loomis, J.B., 2010. The economic cost of adverse health effects from wildfire-smoke exposure: a review. Int. J. Wildland Fire 19 (7), 803–817.
Larjavaara, M., Kuuluvainen, T., Rita, H., 2005. Spatial distribution of lightning-ignited forest fires in Finland. For. Ecol. Manag. 208 (1–3), 177–188.
Lenssen, N.J., Schmidt, G.A., Hansen, J.E., Menne, M.J., Persin, A., Ruedy, R., Zyss, D., 2019. Improvements in the GISTEMP uncertainty model. J. Geophys. Res. Atmos. 124 (12), 6307–6326.
Linley, G.D., Jolly, C.J., Doherty, T.S., Geary, W.L., Armenteras, D., Belcher, C.M., et al., 2022. What do you mean,'megafire'? Global Ecol. Biogeogr. 31 (10), 1906–1922.
Liu, J.C., Pereira, G., Uhl, S.A., Bravo, M.A., Bell, M.L., 2015. A systematic review of the physical health impacts from non-occupational exposure to wildfire smoke. Environ. Res. 136, 120–132.
Luebert, F., Pliscoff, P., 2006. Sinopsis bioclimática y vegetacional de Chile. Editorial Universitaria, Santiago.
McWethy, D.B., Pauchard, A., García, R.A., Holz, A., González, M.E., Veblen, T.T., et al., 2018. Landscape drivers of recent fire activity (2001-2017) in south-central Chile. PLoS One 13 (8), e0201195.
McWethy, D.B., Garreaud, R.D., Holz, A., Pederson, G.T., 2021. Broad-scale surface and atmospheric conditions during large fires in South-Central Chile. Fire 4 (2), 28.
Miranda, A., Altamirano, A., Cayuela, L., Lara, A., González, M., 2017. Native forest loss in the Chilean biodiversity hotspot: revealing the evidence. Reg. Environ. Change 17, 285–297.
Mlawer, E.J., Taubman, S.J., Brown, P.D., Iacono, M.J., Clough, S.A., 1997. Radiative transfer for inhomogeneous atmospheres: RRTM, a validated correlated-k model for the longwave. J. Geophys. Res. Atmos. 102 (D14), 16663–16682.
Montecinos, A., Muñoz, R.C., Oviedo, S., Martínez, A., Villagrán, V., 2017. Climatological characterization of puelche winds down the western slope of the extratropical Andes Mountains using the NCEP Climate Forecast System Reanalysis. J. Appl. Meteorol. Climatol. 56 (3), 677–696.
Myers, N., Mittermeier, R.A., Mittermeier, C.G., Da Fonseca, G.A., Kent, J., 2000. Biodiversity hotspots for conservation priorities. Nature 403 (6772), 853–858.
Nahuelhual, L., Carmona, A., Lara, A., Echeverría, C., González, M.E., 2012. Land-cover change to forest plantations: proximate causes and implications for the landscape in south-central Chile. Landsc. Urban Plann. 107 (1), 12–20.
Nakanishi, M., Niino, H., 2009. Development of an improved turbulence closure model for the atmospheric boundary layer. Journal of the Meteorological Society of Japan. Ser. II 87 (5), 895–912. https://doi.org/10.2151/jmsj.87.895.
National Centers for Environmental Prediction, National Weather Service, NOAA & U.S. Department of Commerce, 2015. NCEP GFS 0.25 degree global forecast grids historical archive. Research Data Archive at the National Center for Atmospheric Research, Computational and Information Systems Laboratory (Updated daily). https://doi.org/10.5065/D65D8PWK. (Accessed 12 December 2023).
Niu, G.Y., Yang, Z.L., Mitchell, K.E., Chen, F., Ek, M.B., Barlage, M., et al., 2011. The community Noah land surface model with multiparameterization options (Noah-MP): 1. Model description and evaluation with local-scale measurements. J. Geophys. Res. Atmos. 116 (D12).
Otto, F.E., 2017. Attribution of weather and climate events. Annu. Rev. Environ. Resour. 42, 627–646.
Pauchard, A., García, R.A., Pena, E., González, C., Cavieres, L.A., Bustamante, R.O., 2008. Positive feedbacks between plant invasions and fire regimes: teline monspessulana (L.) K. Koch (Fabaceae) in central Chile. Biol. Invasions 10, 547–553.
Paveglio, T.B., Brenkert-Smith, H., Hall, T., Smith, A.M., 2015. Understanding social impact from wildfires: advancing means for assessment. Int. J. Wildland Fire 24 (2), 212–224.
Pérez-Invernón, F.J., Gordillo-Vázquez, F.J., Huntrieser, H., Jöckel, P., 2023. Variation of lightning-ignited wildfire patterns under climate change. Nat. Commun. 14 (1), 739.
Philip, S., Kew, S., van Oldenborgh, G.J., Otto, F., Vautard, R., van Der Wiel, K., et al., 2020. A protocol for probabilistic extreme event attribution analyses. Advances in Statistical Climatology, Meteorology and Oceanography 6 (2), 177–203.
Piticar, A., 2018. Changes in heat waves in Chile. Global Planet. Change 169, 234–246. https://doi.org/10.1016/J.GLOPLACHA.2018.08.007.
Pozo, R.A., Galleguillos, M., González, M.E., Vásquez, F., Arriagada, R., 2022. Assessing the socio-economic and land-cover drivers of wildfire activity and its spatiotemporal distribution in south-central Chile. Sci. Total Environ. 810, 152002.
Ramos, A.M., Russo, A., DaCamara, C.C., Nunes, S., Sousa, P., Soares, P.M.M., et al., 2023. The compound event that triggered the destructive fires of October 2017 in Portugal. iScience 26 (3).
Rapanague, M., 2022. Proyecciones del riesgo de incendios forestales en Chile centro-sur bajo distintos escenarios de cambio climático, Master's thesis, Departamento de Geofísica. Universidad de Chile, Santiago, Chile. Available at: https://repositorio.uchile.cl/handle/2250/186900 [In Spanish].
Richardson, D., Black, A.S., Monselesan, D.P., Risbey, J.S., Squire, D.T., Tozer, C.R., Canadell, J.G., 2021. Increased extreme fire weather occurrence in southeast Australia and related atmospheric drivers. Weather Clim. Extrem. 34, 100397.
Rivera, J.A., Arias, P.A., Sörensson, A.A., Zachariah, M., Barnes, C., Philip, S., et al., 2023. 2022 early-summer heatwave in Southern South America: 60 times more likely due to climate change. Climatic Change 176 (8), 102.
Rodrigues, M., Camprubí, À.C., Balaguer-Romano, R., Megía, C.J.C., Castañares, F., Ruffault, J., et al., 2023. Drivers and implications of the extreme 2022 wildfire season in Southwest Europe. Sci. Total Environ. 859, 160320.
Rutllant, J., Garreaud, R., 2004. Episodes of strong flow down the western slope of the subtropical Andes. Mon. Weather Rev. 132 (2), 611–622.
Schulz, J.J., Cayuela, L., Echeverria, C., Salas, J., Benayas, J.M.R., 2010. Monitoring land cover change of the dryland forest landscape of Central Chile (1975–2008). Appl. Geogr. 30 (3), 436–447.
Schumacher, V., Fernández, A., Justino, F., Comin, A., 2020. WRF high resolution dynamical downscaling of precipitation for the Central Andes of Chile and Argentina. Front. Earth Sci. 8, 328.
SENAPRED, 2024a. Balance sobre situación de incendios forestales en el país. Retrieved April 9, 2024 from. https://web.senapred.cl/noticias/balance-sobre-situacion-de-incendios-forestales-en-el-pais/ [In Spanish].
SENAPRED, 2024b. Incendios forestales 2017. Retrieved April 9, 2024 from. https://bibliogrd.senapred.gob [In Spanish].
Skamarock, W.C., Klemp, J.B., 2008. A time-split nonhydrostatic atmospheric model for weather research and forecasting applications. J. Comput. Phys. 227 (7), 3465–3485. https://doi.org/10.1016/j.jcp.2007.01.037.
Skamarock, W.C., Klemp, J.B., Dudhia, J., Gill, D.O., Liu, Z., Berner, J., et al., 2019. A description of the advanced research WRF version 4. NCAR tech. note ncar/tn-556 + str 145. https://doi.org/10.5065/1dfh-6p97.
Srock, A.F., Charney, J.J., Potter, B.E., Goodrick, S.L., 2018. The hot-dry-windy index: a new fire weather index. Atmosphere 9 (7), 279.
Taylor, K.T., Maxwell, B.D., McWethy, D.B., Pauchard, A., Nuñez, M.A., Whitlock, C., 2017. Pinus contorta invasions increase wildfire fuel loads and may create a positive feedback with fire. Ecology 98 (3), 678–687.
Thompson, G., Field, P.R., Rasmussen, R.M., Hall, W.D., 2008. Explicit forecasts of winter precipitation using an improved bulk microphysics scheme. Part II: implementation of a new snow parameterization. Mon. Weather Rev. 136 (12), 5095–5115. https://doi.org/10.1175/2008MWR2387.1.
Turco, M., Jerez, S., Augusto, S., Tarín-Carrasco, P., Ratola, N., Jiménez-Guerrero, P., Trigo, R.M., 2019. Climate drivers of the 2017 devastating fires in Portugal. Sci. Rep. 9 (1), 13886.
Turney, F.A., Saide, P.E., Jimenez Munoz, P.A., Muñoz-Esparza, D., Hyer, E.J., Peterson, D.A., et al., 2023. Sensitivity of burned area and fire radiative power predictions to containment efforts, fuel density, and fuel moisture using WRF-fire. J. Geophys. Res. Atmos. 128 (18), e2023JD038873.
Urrutia-Jalabert, R., González, M.E., González-Reyes, Á., Lara, A., Garreaud, R., 2018. Climate variability and forest fires in central and south-central Chile. Ecosphere 9 (4), e02171.
Viale, M., Garreaud, R., 2014. Summer precipitation events over the western slope of the subtropical Andes. Mon. Weather Rev. 142 (3), 1074–1092.
Weber, K.T., Yadav, R., 2020. Spatiotemporal trends in wildfires across the Western United States (1950–2019). Rem. Sens. 12 (18), 2959.
Wheeler, M.C., Hendon, H.H., 2004. An all-season real-time multivariate MJO index: development of an index for monitoring and prediction. Mon. Weather Rev. 132 (8), 1917–1932.
Wierzchowski, J., Heathcott, M., Flannigan, M.D., 2002. Lightning and lightning fire, central cordillera, Canada. Int. J. Wildland Fire 11 (1), 41–51.
Williams, A.P., Abatzoglou, J.T., Gershunov, A., Guzman-Morales, J., Bishop, D.A., Balch, J.K., Lettenmaier, D.P., 2019. Observed impacts of anthropogenic climate change on wildfire in California. Earth's Future 7 (8), 892–910.
Xu, R., Yu, P., Abramson, M.J., Johnston, F.H., Samet, J.M., Bell, M.L., et al., 2020. Wildfires, global climate change, and human health. N. Engl. J. Med. 383 (22), 2173–2181.
Yáñez-Morroni, G., Gironás, J., Caneo, M., Delgado, R., Garreaud, R., 2018. Using the Weather Research and Forecasting (WRF) model for precipitation forecasting in an Andean region with complex topography. Atmosphere 9 (8), 304.
Youssouf, H., Liousse, C., Roblou, L., Assamoi, E.M., Salonen, R.O., Maesano, C., et al., 2014. Non-accidental health impacts of wildfire smoke. Int. J. Environ. Res. Publ. Health 11 (11), 11772–11804.